

Printing ferromagnetic domains for untethered fast-transforming soft materials

Yoonho Kim^{1,2,5}, Hyunwoo Yuk^{1,5}, Ruike Zhao^{1,5}, Shawn A. Chester³ & Xuanhe Zhao^{1,4*}

Soft materials capable of transforming between three-dimensional (3D) shapes in response to stimuli such as light, heat, solvent, electric and magnetic fields have applications in diverse areas such as flexible electronics^{1,2}, soft robotics^{3,4} and biomedicine^{5–7}. In particular, magnetic fields offer a safe and effective manipulation method for biomedical applications, which typically require remote actuation in enclosed and confined spaces^{8–10}. With advances in magnetic field control¹¹, magnetically responsive soft materials have also evolved from embedding discrete magnets¹² or incorporating magnetic particles¹³ into soft compounds to generating nonuniform magnetization profiles in polymeric sheets^{14,15}. Here we report 3D printing of programmed ferromagnetic domains in soft materials that enable fast transformations between complex 3D shapes via magnetic actuation. Our approach is based on direct ink writing¹⁶ of an elastomer composite containing ferromagnetic microparticles. By applying a magnetic field to the dispensing nozzle while printing¹⁷, we reorient particles along the applied field to impart patterned magnetic polarity to printed filaments. This method allows us to program ferromagnetic domains in complex 3D-printed soft materials, enabling a set of previously inaccessible modes of transformation, such as remotely controlled auxetic behaviours of mechanical metamaterials with negative Poisson's ratios. The actuation speed and power density of our printed soft materials with programmed ferromagnetic domains are orders of magnitude greater than existing 3D-printed active materials. We further demonstrate diverse functions derived from complex shape changes, including reconfigurable soft electronics, a mechanical metamaterial that can jump and a soft robot that crawls, rolls, catches fast-moving objects and transports a pharmaceutical dose.

Our composite ink for 3D printing consists of magnetizable microparticles of neodymium–iron–boron (NdFeB) alloy (Extended Data Fig. 1a) and fumed silica nanoparticles (Extended Data Fig. 1b) embedded in a silicone rubber matrix containing silicone catalyst and crosslinker (Fig. 1a). The fumed silica within the silicone resin serves as a rheological modifier to induce the mechanical properties required for direct ink writing^{3,16} including shear thinning (Extended Data Fig. 2a) and shear yielding (Extended Data Fig. 2b). These properties ensure that the composite ink can be extruded through a micro-nozzle when pressurized and that the deposited inks maintain their shapes even when stacked up to form multiple layers. The composite ink is prepared first by mixing the non-magnetized NdFeB particles and the silica nanoparticles with the uncured elastomer matrix and then magnetized to saturation under an impulse field (about 2.7 T). The presence of yield stress in the composite ink helps to prevent the dispersed magnetized particles from agglomerating (Extended Data Fig. 3a).

During the printing process, a magnetic field is applied along (or in reverse to) the flow direction of the ink via a permanent magnet or an electromagnetic coil placed around the dispensing nozzle (Fig. 1a). The applied field makes the magnetized NdFeB particles reorient along the field direction, imparting a permanent magnetic moment to the extruded ink filament. The magnetic polarities of the deposited inks

can be tuned either by switching the applied field direction or changing the printing direction. Using this approach, a 3D structure can be encoded with intricate patterns of ferromagnetic domains depending on the magnetic polarities of the filaments that are arranged to construct the 3D structure. To avoid interference in the programmed domains of the printed structure by the applied field at the nozzle, a magnetic shield is used to attenuate the magnetic flux density under the nozzle tip (Fig. 1a). When the printing process is complete, the printed structure is cured at 120 °C for 1 h, during which the presence of yield stress in the uncured ink helps the programmed ferromagnetic domains to remain unaffected by thermal randomization of the aligned particles.

To evaluate the efficacy of our method in printing ferromagnetic domains, we measure the magnetic moment density, or magnetization, in samples (Extended Data Fig. 4) printed under various conditions including the magnetic particle content, the applied field strength and the nozzle diameter. First, samples are printed with magnetic inks containing different volume fractions of NdFeB particles through a nozzle with diameter 410 μm under a magnetic field of 50 mT at the nozzle tip. The measured magnetic moment density varies almost linearly from 16 kA m^{-1} to 81 kA m^{-1} as the volume fraction of NdFeB particles in the composite ink increases from 5% to 20% (Fig. 1b). Next, as the applied field at the nozzle tip increases from 20 mT to 50 mT, the magnetic moment density of printed samples (with 20 vol% NdFeB particles through nozzles with diameter 410 μm) increases from 68 kA m^{-1} to 81 kA m^{-1} (Fig. 1c). When the nozzle diameter varies from 200 μm to 1,190 μm , the magnetic moment density of printed samples (with 20 vol% NdFeB particles under a magnetic field of 50 mT at the nozzle tip) increases from 76.6 kA m^{-1} to 85.4 kA m^{-1} (Fig. 1d). When printed with very fine nozzles (with diameters of 50 μm and 100 μm), the fibre diameter becomes larger than the nozzle diameter owing to the die-swelling effect (Extended Data Fig. 1c, d). The ratio between the fibre and nozzle diameters decreases as the nozzle diameter increases, reaching almost one when the nozzle diameter is larger than 200 μm (Extended Data Fig. 1e–g). Printing in the absence of external magnetic fields yields magnetization values below 5 kA m^{-1} for all nozzle diameters, because the particles are randomly oriented. Furthermore, we print samples in the absence of external field and then magnetize them under impulse fields (about 2.7 T) after curing, which yields the maximum achievable magnetic moment density at each volume fraction of NdFeB particles. In comparison, printing under magnetic fields of 50 mT yields a magnetic moment density that corresponds to about 63–64% of the maximum achievable value at the same concentration of NdFeB particles (Extended Data Fig. 5).

We develop a model to predict the transformation of complex 3D-printed structures with programmed ferromagnetic domains under magnetic fields. Application of magnetic fields induces torques on the embedded ferromagnetic particles, which create stresses that collectively lead to a macroscale material response. If the magnetic moment density (magnetization), a vector quantity, is \mathbf{M} at a certain point of an incompressible body in the reference configuration, the magnetization vector at the same material point in the deformed body

¹Soft Active Materials Laboratory, Department of Mechanical Engineering, Massachusetts Institute of Technology, Cambridge, MA, USA. ²Harvard-MIT Division of Health Sciences and Technology, Massachusetts Institute of Technology, Cambridge, MA, USA. ³Department of Mechanical and Industrial Engineering, New Jersey Institute of Technology, Newark, NJ, USA. ⁴Department of Civil and Environmental Engineering, Massachusetts Institute of Technology, Cambridge, MA, USA. ⁵These authors contributed equally: Yoonho Kim, Hyunwoo Yuk, Ruike Zhao. *e-mail: xzhao@mit.edu

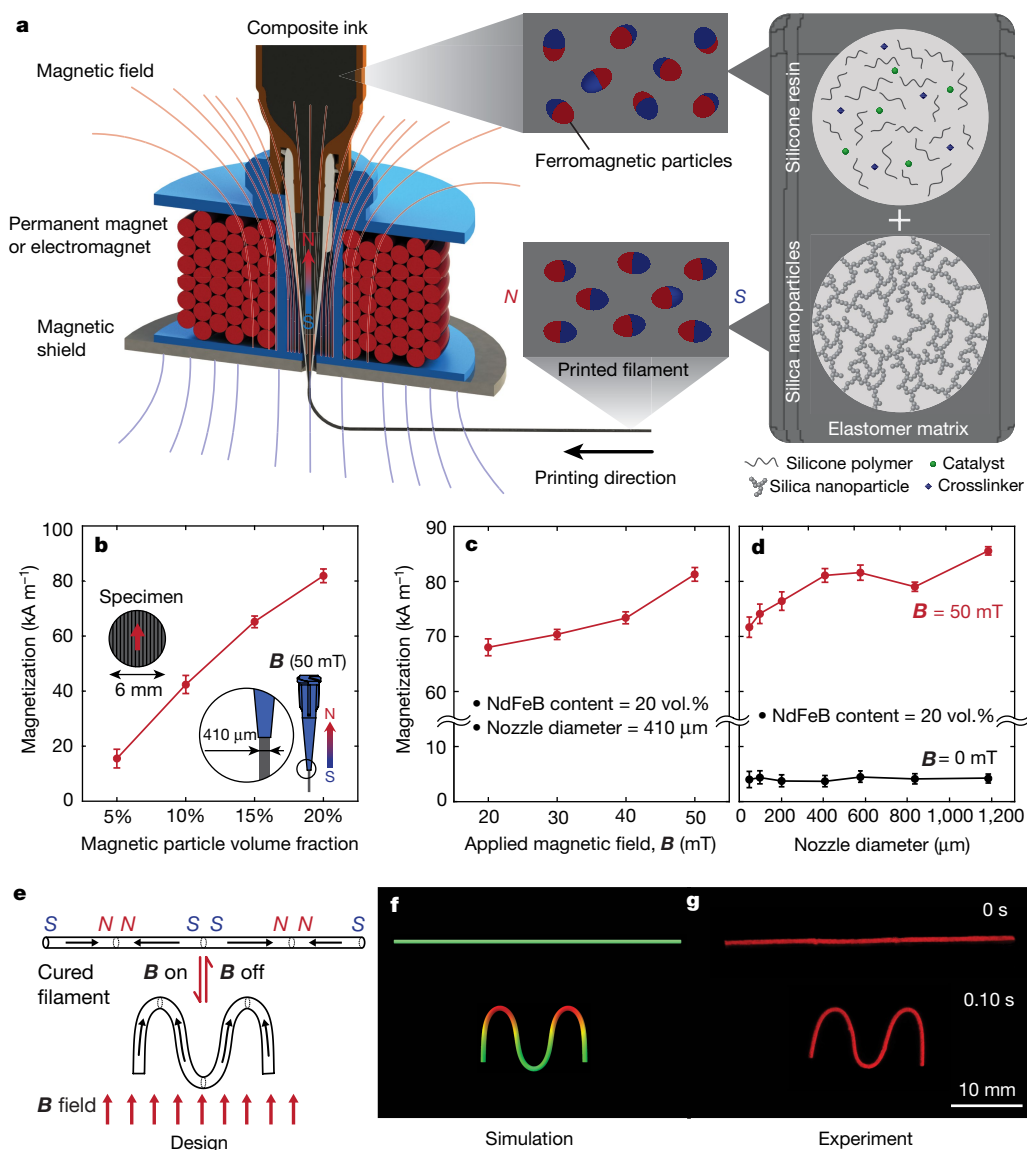


Fig. 1 | Design of ferromagnetic domains in 3D-printed soft materials. **a**, Schematics of the printing process and the material composition. The ferromagnetic particles embedded in the composite ink are reoriented by the applied magnetic field generated by a permanent magnet or an electromagnet placed around the dispensing nozzle. **b**, Effect of the volume fraction of magnetized NdFeB particles in the ink on the magnetization of printed samples. **c**, Effect of the applied field strength around the nozzle on the magnetization of printed samples. **d**, Effect of nozzle diameter on the magnetization of printed samples. Samples printed in the absence of applied magnetic fields give magnetization values below 5 kA m^{-1} . Error

bars indicate the standard deviation for $n = 3$ measurements at each data point. **e–g**, Schematic illustration (**e**), simulation of the finite-element model (**f**) and experimental results (**g**) of a single fibre encoded with alternating magnetic domains designed to form an 'm' shape in 0.1 s under an applied magnetic field of 200 mT. The elastomeric fibre is printed using a nozzle of diameter 840 μm while switching the direction of magnetic fields (50 mT at the nozzle tip) generated by an electromagnetic coil that encompasses the nozzle. All samples discussed in **c**, **d** and **g** are prepared with the elastomeric composite ink containing 20 vol% of magnetized NdFeB particles.

can be expressed as \mathbf{FM} , where \mathbf{F} denotes the deformation gradient tensor at the point. Then, the magnetic potential energy per unit reference volume under an applied magnetic field \mathbf{B} can be expressed as $W^{\text{magnetic}} = -\mathbf{FM} \cdot \mathbf{B}$, under the assumptions that the presence of soft materials does not substantially alter the applied field and that the potential energy from higher-order terms of \mathbf{B} and \mathbf{M} are negligible. From the magnetic potential energy density, the Cauchy stress tensor induced by the applied field on the magnetic moments can be calculated as $\sigma^{\text{magnetic}} = -\mathbf{B} \otimes \mathbf{FM}$, where the operation \otimes denotes the dyadic product, which takes two vectors to yield a second-order tensor. To simulate the deformation of complex structures programmed with ferromagnetic domains, the magnetic stress tensor is implemented as a user-defined element subroutine in the commercial finite-element analysis software ABAQUS (details are available in Supplementary Information).

As an illustrative example to demonstrate the ability to program ferromagnetic domains, a straight filament is printed with an alternating magnetization pattern as illustrated in Fig. 1e by switching the applied field direction during the printing. Upon application of a uniform magnetic field of 200 mT, the straight filament transforms into an 'm' shape in 0.1 s (Fig. 1g), and quickly reverts to its original shape upon removal of the applied field in 0.2 s. Such rapid, reversible transformation can be repeated on demand by magnetic actuation (Supplementary Video 1). The simulation conducted under the same conditions, including the magnetic and mechanical properties and the applied field as in the experiment, is in good agreement with the experimental results (Fig. 1f), validating the use of model-based simulation to guide the design of complex shape-morphing structures with programmed ferromagnetic domains.

In Fig. 2, we present a set of two-dimensional planar structures that rapidly transform into complex 3D shapes under the applied magnetic

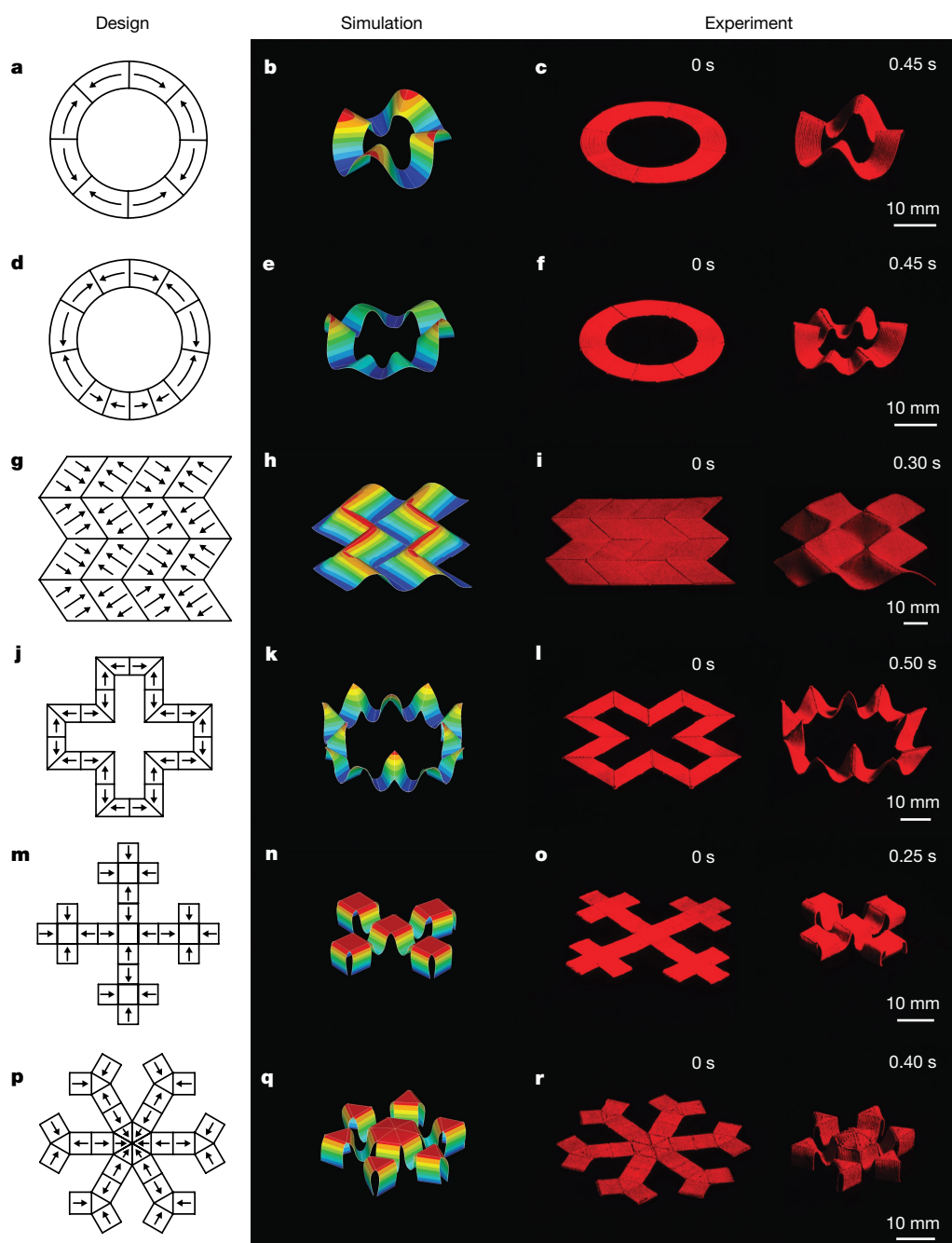


Fig. 2 | Various two-dimensional planar structures with programmed ferromagnetic domains demonstrating complex shape changes under applied magnetic fields. **a–r**, Schematic designs, finite-element simulations and experimental results for an annulus encoded with alternating domains that are equidistant (**a–c**); an annulus encoded with alternating domains that vary in size (**d–f**); a Miura-ori fold encoded with alternating oblique patterns of ferromagnetic domains (**g–i**); a hollow cross encoded with alternating ferromagnetic domains along the perimeter (**j–l**); quadrupedal (**m–o**) and hexapedal (**p–r**) structures enabled by

folding of the magnetically active segments surrounding the magnetically inactive segments (unlabelled areas in the schematic designs). All of the demonstrated structures are printed with the elastomeric composite ink containing 20 vol% of magnetized NdFeB particles using a nozzle of diameter 410 μm under a magnetic field of 50 mT at the nozzle tip generated by a permanent magnet. Actuation of the demonstrated structures is performed by applying magnetic fields of 200 mT perpendicular to the planes of the structures. The detailed dimensions of the printed structures are given in Extended Data Fig. 6a–f.

fields of 200 mT as a result of the programmed ferromagnetic domains. In Fig. 2a and d, we design two annular rings with the same geometry but different patterns of ferromagnetic domains to illustrate the effects of programmed domains on the macroscale response. Our model-based simulation predicts that the two rings should yield different 3D morphologies under the same magnetic field applied perpendicularly to their planes. The second annulus encoded with alternating patterns that vary in magnitude gives a more complex undulating shape (Fig. 2e) than does the first annulus (Fig. 2b), whose alternating patterns are

equidistant. The simulation results are in good agreement with experimental results (Fig. 2c, f, Supplementary Video 2), further demonstrating that our model is capable of guiding the design of complex shape-morphing structures using programmed ferromagnetic domains.

When programmed with more intricate domain patterns, even a simple geometry can yield a complex 3D shape under an applied magnetic field. As an example, in Fig. 2g, we design a simple rectangular structure with alternating oblique patterns of ferromagnetic domains to create a Miura-ori pattern¹⁸. This untethered structure provides fast

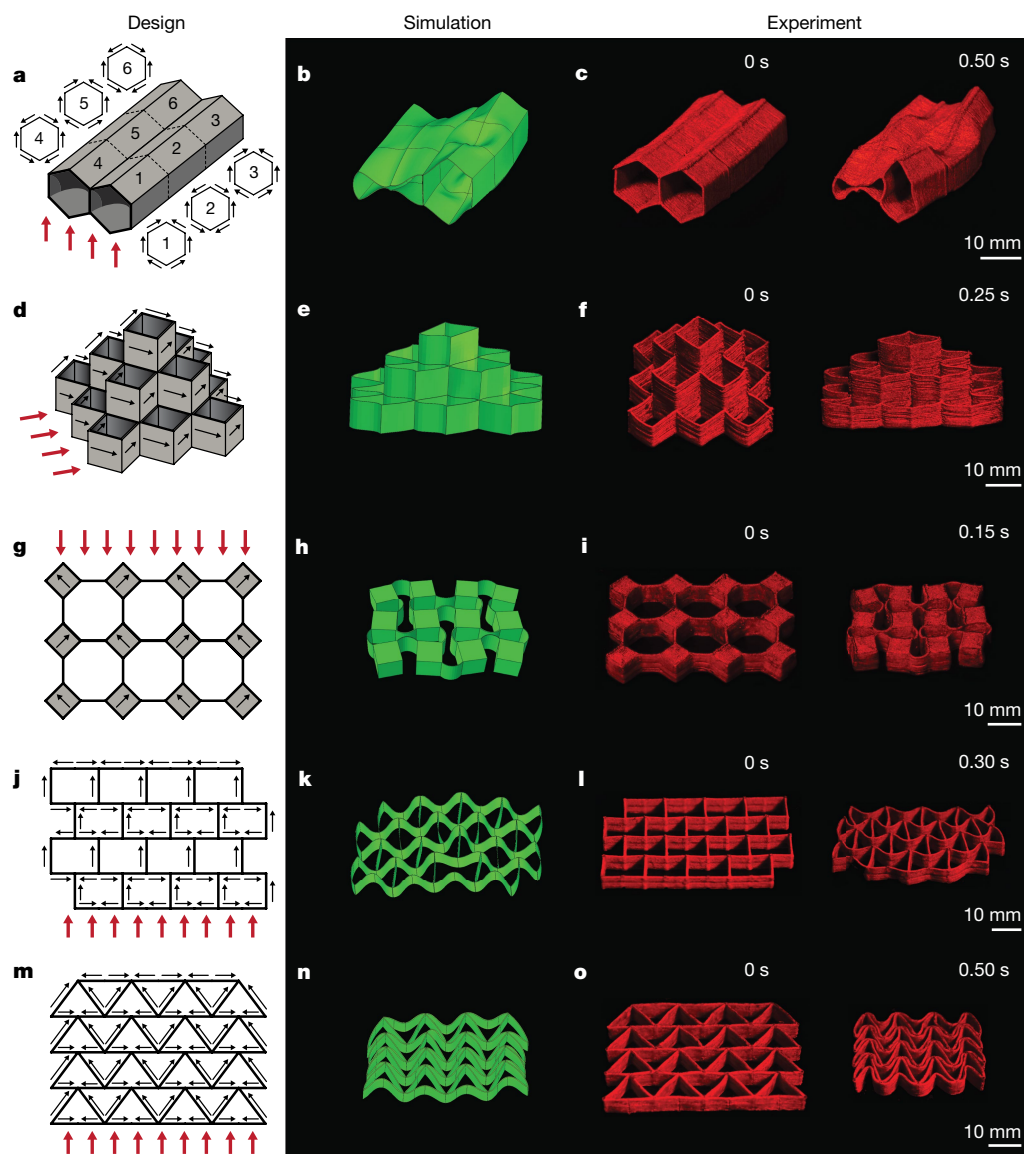


Fig. 3 | Various 3D structures with programmed ferromagnetic domains demonstrating complex shape changes under applied magnetic fields. **a–o**, Schematic designs, finite-element simulations and experimental results for two adjoining hexagonal tubes programmed to form undulating surfaces under the applied magnetic field owing to the alternating ferromagnetic domains (**a–c**); a pyramid-shaped thin-walled structure exhibiting elongation in its diagonal direction along the applied magnetic field (**d–f**); a set of auxetic structures (with negative Poisson's

ratios) exhibiting shrinkage in both length and width under applied magnetic fields (**g–o**). All of the demonstrated structures are printed with elastomeric composite ink containing 20 vol% of magnetized NdFeB particles using a nozzle of diameter 410 μm under a magnetic field of 50 mT at the nozzle tip, generated by a permanent magnet. Actuation of the demonstrated structures is performed by applying magnetic fields of 200 mT along the directions indicated in **a**, **d**, **g**, **j** and **m**. The detailed dimensions of the printed structures are given in Extended Data Fig. 6g–k.

(in 0.3 s) and fully reversible folding and unfolding under magnetic actuation (Fig. 2i and Supplementary Video 2), as predicted by our model (Fig. 2h). Notably, the response speed of our Miura-ori structure with programmed ferromagnetic domains is much faster than existing ones in the literature based on liquid crystal elastomers^{19,20}, shape memory polymers^{21,22} and thermally responsive hydrogels²³.

When more intricate designs are programmed with ferromagnetic domains, as illustrated in Fig. 2j, m and p, the two-dimensional planar structures transform into more complex 3D shapes (Fig. 2l, o, r and Supplementary Video 2); for these it is no longer straightforward to trace the original shapes without knowing the programmed domains. Design and realization of such complex shape-morphing structures are enabled by the model-based simulations, which accurately predict the complex 3D morphologies (Fig. 2k, n, q and Supplementary Video 2). Previously, a transition from two-dimensional planar structures to complex 3D shapes has been achieved by controlled buckling of materials that are selectively attached on biaxially stretched

elastomeric substrates^{24,25}. Compared with existing techniques, our method based on printing ferromagnetic domains offers additional advantages in two-dimensional to 3D structural transition, including (i) substrate-free, remote actuation, (ii) fast and fully reversible transformation and (iii) the capability to selectively actuate specific parts of the structure.

Our method of printing ferromagnetic domains can be further extended to complex 3D structures. When printing 3D structures with direct ink writing, however, difficulties typically arise owing to structural instability as the deposited filaments are stacked up. To ensure a more stable printing process, we introduce a support ink composed of a silicone resin containing catalyst and fumed silica nanoparticles (Extended Data Fig. 7; see Extended Data Fig. 2a and b for rheological properties). When printed, the support ink serves as a fugitive support that buttresses the adjacent magnetic ink (Extended Data Fig. 7a and Supplementary Video 3). After the magnetic ink is fully cured, the support ink can be removed by solvent rinses (Extended Data Fig. 7c).

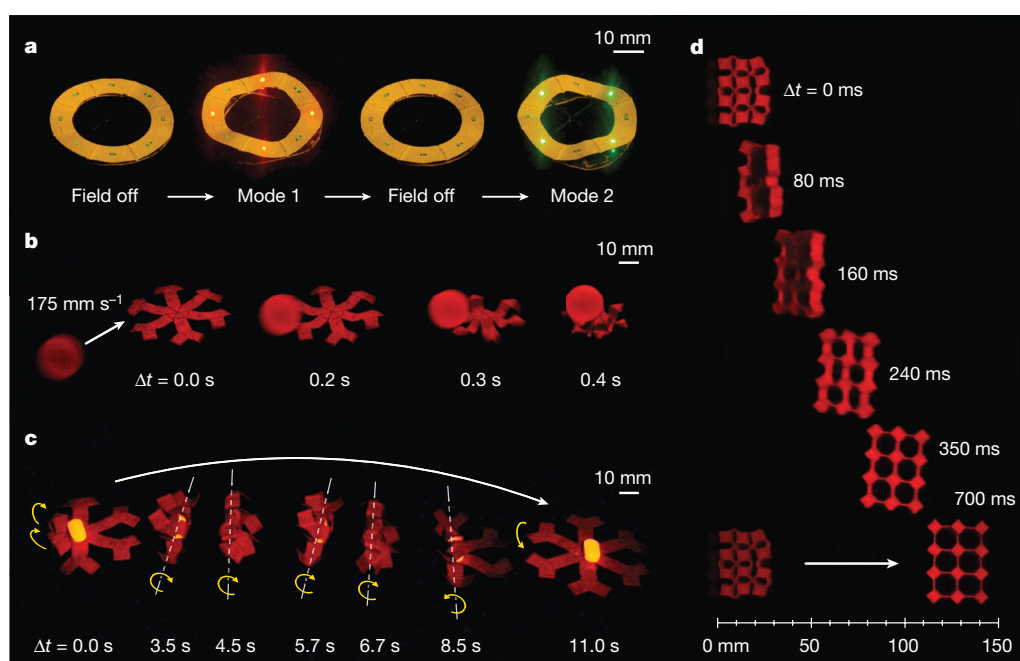


Fig. 4 | Functional demonstrations of 3D-printed soft materials with programmed ferromagnetic domains. **a**, A reconfigurable soft electronic device (as detailed in Extended Data Fig. 9) based on the annular ring structure exhibiting different electronic functions depending on the direction of an applied magnetic field of 30 mT. **b**, A hexapedal structure stopping and holding a fast-moving object (glass ball of diameter 18 mm and weight 8 g) upon application of a magnetic field generated

by a permanent magnet. **c**, A hexapedal structure wrapping an oblong pharmaceutical pill and carrying the pill using rolling-based locomotion under a rotating magnetic field generated by a permanent magnet. **d**, Horizontal leap of a 3D auxetic structure upon sudden reversal of the applied magnetic field direction while attenuating the field strength by rotating a permanent magnet by 90°. Detailed information on how to apply the magnetic fields to achieve actuation is given in Extended Data Fig. 10.

The use of support ink and the consequent ability to print 3D structures with programmed domains allow us to create a set of high-aspect-ratio multilayered structures (Fig. 3) that exhibit rapid and reversible transformation between complex 3D shapes under magnetic fields of 200 mT. In Fig. 3c, we present a thin-walled structure consisting of two adjoining hexagonal tubes with high aspect ratios. The ferromagnetic domains are programmed in such a way that some parts of the tubes expand while the others collapse, as illustrated in Fig. 3a, to create complex undulating surfaces in a continuous 3D structure under the applied magnetic field, as predicted and observed by the simulation and the experiment (Fig. 3b, c and Supplementary Video 4), respectively. In another example, to demonstrate the versatility of our fabrication method, we create a pyramid-shaped thin-walled structure that elongates along the direction of applied magnetic fields (Fig. 3e, f and Supplementary Video 4) as a result of the programmed magnetic domains (Fig. 3d).

The versatility of our model-guided design and fabrication method enables us to create auxetic structures (Fig. 3i, l, o), a type of mechanical metamaterials characterized by negative Poisson's ratios. Our printed auxetic structures exhibit shrinkage in both length and width in response to external magnetic fields. Typically, mechanical metamaterials show auxetic behaviours only when uniaxially compressed or stretched and thus require direct mechanical contact²⁶. In addition, owing to the limited fabrication techniques available to achieve complex designs, remote actuation of untethered auxetic structures has not been realized in other types of active materials. Guided by our model-based predictions (Fig. 3h, k, n), we design a set of mechanical metamaterials with programmed ferromagnetic domains (Fig. 3g, j, m) that quickly shrink in both length and width under the applied fields within 0.5 s and recover their original shapes upon removal of the applied fields (Fig. 3i, l, o and Supplementary Video 5). The use of magnetic fields as an actuation method obviates the need for direct contact in realizing auxetic behaviours in mechanical metamaterials.

In the design and fabrication of shape-programmable soft materials, intensive efforts have been made to increase the level of complexity by

adopting 3D printing techniques such as inkjet printing²⁷, stereolithography^{28,29} and direct ink writing³⁰. However, fast and fully reversible actuation between programmed shapes has remained a central challenge in the field. To quantitatively evaluate the actuation performance, we compare the energy density and the actuation rate (Extended Data Fig. 8a) of printed shape-programmable materials in the literature. We also compare the power density (Extended Data Fig. 8b), one often-used metric to evaluate the actuation performance of active materials. Our shape-morphing structures shown in Figs. 2 and 3 deform up to strain levels from 0.15 to 0.25 within 0.1 s to 0.5 s, providing a power density ranging from 22.3 kW m⁻³ to 309.3 kW m⁻³, which are orders of magnitude greater than the actuation rates and power densities achieved by existing 3D-printed shape-transforming soft materials.

The capability to create complex shape changes allows us to achieve diverse functions from our printed structures, as shown in Fig. 4. First, by combining electronic components and circuitry with our annular ring structure in Fig. 2c, we print a soft electronic device as detailed in Extended Data Fig. 9a. This soft electronic device deforms into two different shapes depending on the direction of applied magnetic fields of 30 mT, and each mode of transformation yields a different electronic function (Fig. 4a, Extended Data Fig. 9b, c and Supplementary Video 6). The results demonstrate that our multimaterial 3D printing method gives functionally reconfigurable soft electronic devices, whose rigid-material counterparts have recently been achieved by means of multistable buckling³¹.

We further demonstrate the capability of interacting with an object based on the complex shape changes of the hexapedal structure shown in Fig. 2r. Using the fast response upon magnetic actuation, the hexapedal structure quickly stops a fast-moving object (Fig. 4b and Supplementary Video 7). When applying a magnetic field in the opposite direction to create a reversed shape, the hexapedal structure can catch a falling object and hold it against external disturbance and then release the object on demand by using the previous mode of transformation (Supplementary Video 7). When a rotating magnetic field is applied, the hexapedal structure can roll up its body and move

forwards and backwards by rolling-based locomotion (Supplementary Video 8). Harnessing the shape changes and motion, the hexapedal structure can carry an object with arbitrary shape such as a round or oblong pharmaceutical pill (Fig. 4c) and release the pill on demand (Supplementary Video 8).

The 3D mechanical metamaterial presented in Fig. 3i can show a horizontal leap based on the drastic release of the elastic and magnetic potential energy (Fig. 4d and Supplementary Video 9). The fast response of the auxetic structure generates an average speed of 250 mm s^{-1} during the leap, allowing it to move forwards by 120 mm within 0.7 s on the horizontal plane. This leaping motion is achieved by first applying a magnetic field in one direction to collapse the auxetic structure and then switching to a field in the opposite direction while attenuating the field strength. This sudden reversal of the field direction quickly increases the magnetic potential energy and triggers the drastic release of the stored elastic and magnetic potential energy, which is converted to kinetic energy during the horizontal leap.

Our printing method as a fabrication platform can be extended to multiple composite inks using different types of elastomer and hydrogel matrices and magnetic particles. By printing ferromagnetic domains in soft materials, we introduce new design parameters—domain patterns, magnetization strength and actuation fields—into the design and fabrication of shape-programmable soft materials. The remote actuation of such untethered, complex and fast shape-shifting soft materials based on magnetic fields suggests new possibilities for applications in flexible electronics, biomedical devices and soft robotics.

Online content

Any Methods, including any statements of data availability and Nature Research reporting summaries, along with any additional references and Source Data files, are available in the online version of the paper at <https://doi.org/10.1038/s41586-018-0185-0>.

Received: 22 November 2017; Accepted: 11 April 2018;

Published online 13 June 2018.

- Ma, M., Guo, L., Anderson, D. G. & Langer, R. Bio-inspired polymer composite actuator and generator driven by water Gradients. *Science* **339**, 186–189 (2013).
- Zarek, M. et al. 3D printing of shape memory polymers for flexible electronic devices. *Adv. Mater.* **28**, 4449–4454 (2016).
- Wehner, M. et al. An integrated design and fabrication strategy for entirely soft, autonomous robots. *Nature* **536**, 451–455 (2016).
- Park, S. J. et al. Phototactic guidance of a tissue-engineered soft-robotic ray. *Science* **353**, 158–162 (2016).
- Zhao, X. H. et al. Active scaffolds for on-demand drug and cell delivery. *Proc. Natl Acad. Sci. USA* **108**, 67–72 (2011).
- Fusco, S. et al. An integrated microrobotic platform for on-demand, targeted therapeutic interventions. *Adv. Mater.* **26**, 952–957 (2014).
- Davis, K. A., Burke, K. A., Mather, P. T. & Henderson, J. H. Dynamic cell behavior on shape memory polymer substrates. *Biomaterials* **32**, 2285–2293 (2011).
- Erb, R. M., Martin, J. J., Soheilani, R., Pan, C. & Barber, J. R. Actuating soft matter with magnetic torque. *Adv. Funct. Mater.* **26**, 3859–3880 (2016).
- Hines, L., Petersen, K., Lum, G. Z. & Sitti, M. Soft actuators for small-scale robotics. *Adv. Mater.* **29**, 1603483 (2017).
- Martel, S. Beyond imaging: macro- and microscale medical robots actuated by clinical MRI scanners. *Science Robotics* **2**, eaam8119 (2017).
- Rahmer, J., Stehning, C. & Gleich, B. Spatially selective remote magnetic actuation of identical helical micromachines. *Science Robotics* **2**, eaal2845 (2017).
- Boncheva, M. et al. Magnetic self-assembly of three-dimensional surfaces from planar sheets. *Proc. Natl Acad. Sci. USA* **102**, 3924–3929 (2005).
- Kim, J., Chung, S., Choi, S., Lee, H. & Kwon, S. Programming magnetic anisotropy in polymeric microactuators. *Nat. Mater.* **10**, 747–752 (2011).
- Lum, G. Z. et al. Shape-programmable magnetic soft matter. *Proc. Natl Acad. Sci. USA* **113**, E6007–E6015 (2016).
- Hu, W., Lum, G. Z., Mastrangeli, M. & Sitti, M. Small-scale soft-bodied robot with multimodal locomotion. *Nature* **554**, 81–85 (2018).
- Lewis, J. A. Direct ink writing of 3D functional materials. *Adv. Funct. Mater.* **16**, 2193–2204 (2006).
- Kokkinis, D., Schaffner, M. & Studart, A. R. Multimaterial magnetically assisted 3D printing of composite materials. *Nat. Commun.* **6**, 8643 (2015).
- Silverberg, J. L. et al. Using origami design principles to fold reprogrammable mechanical metamaterials. *Science* **345**, 647–650 (2014).
- Yuan, C. et al. 3D printed reversible shape changing soft actuators assisted by liquid crystal elastomers. *Soft Matter* **13**, 5558–5568 (2017).
- Ware, T. H., McConney, M. E., Wie, J. J., Tondiglia, V. P. & White, T. J. Voxelated liquid crystal elastomers. *Science* **347**, 982–984 (2015).
- Oyefusi, A. & Chen, J. Reprogrammable chemical 3D shaping for origami, kirigami, and reconfigurable molding. *Angew. Chem.* **129**, 8362–8365 (2017).
- Zhao, Z. et al. Origami by frontal photopolymerization. *Sci. Adv.* **3**, e1602326 (2017).
- Na, J. H. et al. Programming reversibly self-folding origami with micropatterned photo-crosslinkable polymer trilayers. *Adv. Mater.* **27**, 79–85 (2015).
- Xu, S. et al. Assembly of micro/nanomaterials into complex, three-dimensional architectures by compressive buckling. *Science* **347**, 154–159 (2015).
- Zhang, Y. H. et al. A mechanically driven form of kirigami as a route to 3D mesostructures in micro/nanomembranes. *Proc. Natl Acad. Sci. USA* **112**, 11757–11764 (2015).
- Babaei, S. et al. 3D soft metamaterials with negative Poisson's ratio. *Adv. Mater.* **25**, 5044–5049 (2013).
- Ding, Z. et al. Direct 4D printing via active composite materials. *Sci. Adv.* **3**, e1602890 (2017).
- Kim, J., Hanna, J. A., Byun, M., Santangelo, C. D. & Hayward, R. C. Designing responsive buckled surfaces by halftone gel lithography. *Science* **335**, 1201–1205 (2012).
- Ge, Q. et al. Multimaterial 4D printing with tailorable shape memory polymers. *Sci. Rep.* **6**, 31110 (2016).
- Gladman, A. S., Matsumoto, E. A., Nuzzo, R. G., Mahadevan, L. & Lewis, J. A. Biomimetic 4D printing. *Nat. Mater.* **15**, 413–418 (2016).
- Fu, H. et al. Morphable 3D mesostructures and microelectronic devices by multistable buckling mechanics. *Nat. Mater.* **17**, 268–276 (2018).

Acknowledgements We thank D. Bono for help in magnetic characterizations. This work is supported by the National Science Foundation (CMMI-1661627) and the Office of Naval Research (N00014-17-1-2920) and the MIT Institute for Soldier Nanotechnologies. Y.K. acknowledges financial support from Harvard-MIT Division of Health Sciences and Technology. H.Y. acknowledges financial support from a Samsung Scholarship.

Author contributions Y.K., H.Y., R.Z. and X.Z. designed the study and interpreted the results. H.Y., Y.K. and X.Z. conceived the idea of printing ferromagnetic domains. H.Y. and X.Z. developed the 3D printing platform. Y.K. and H.Y. developed materials and methods of printing and performed material characterizations. Y.K. designed and fabricated the printed structures and demonstrated their functions. X.Z., R.Z. and Y.K. developed the theory for soft materials with ferromagnetic domains, R.Z. and S.A.C. implemented the numerical models, and R.Z. performed the simulations. Y.K., H.Y. and R.Z. produced the figures and videos. Y.K. and X.Z. wrote the manuscript with input from all authors. X.Z. supervised the study.

Competing interests The authors declare no competing interests.

Additional information

Extended data is available for this paper at <https://doi.org/10.1038/s41586-018-0185-0>.

Supplementary information is available for this paper at <https://doi.org/10.1038/s41586-018-0185-0>.

Reprints and permissions information is available at <http://www.nature.com/reprints>.

Correspondence and requests for materials should be addressed to X.Z.

Publisher's note Springer Nature remains neutral with regard to jurisdictional claims in published maps and institutional affiliations.

METHODS

Ink composition and preparation. The magnetic ink was prepared first by blending two silicone-based materials—SE 1700 (Dow Corning Corp.) and Ecoflex 00-30 Part B (Smooth-on Inc.)—in a 1:2 volume ratio. Ecoflex 00-30 Part B, a softer elastomer than SE 1700, was used to achieve the preferred mechanical properties of the composite material. Fumed silica nanoparticles (amorphous, 20–30 nm; US Research Nanomaterials Inc.), which corresponds to 12.5 wt% with respect to Ecoflex Part B, were added to achieve required rheological properties for direct ink writing. After mixing the blend in a planetary mixer (AR-100, Thinky) at 2,000 r.p.m. for 2 min, 20 vol% NdFeB microparticles (287.5 wt% with respect to Ecoflex Part B) with an average size of 5 μm (MQFP-B-2007609-089, Magnequench) were added into the elastomer mixture and then mixed thoroughly at 2,000 r.p.m. for 3 min, followed by defoaming at 2,200 r.p.m. for 1 min. The composite ink was then magnetized by impulse magnetic fields (about 2.7 T) generated by an impulse magnetizer (IM-10-30, ASC Scientific) to impart magnetic polarities to the ferromagnetic particles embedded in the elastomer matrix. Both SE 1700 and Ecoflex 00-30 are platinum-catalysed, addition-curing silicones, so 10 wt% SE 1700 catalyst with respect to SE 1700 base was added into the magnetized ink and then mixed at 2,000 r.p.m. for 30 s before printing. The final concentrations of components were as follows: 21.78 wt% Ecoflex 00-30 Part B, 2.72 wt% fumed silica nanoparticles, 11.71 wt% SE 1700 base, 1.17 wt% SE 1700 catalyst and 62.62 wt% NdFeB microparticles. For imaging purposes, about 2 wt% fluorescent colourants (Ignite PMS 805C, Smooth-on Inc.) were added to this final composition.

The support ink, which was used for supporting structures when printing multilayered or 3D structures with the magnetic ink, was prepared by mixing a platinum-based silicone-curing accelerator (Elastosil CAT PT-F, Wacker) with fumed silica nanoparticles (amorphous, 20–30 nm; US Research Nanomaterials Inc.) in a 5.45:1 mass ratio. Fumed silica nanoparticles were added to achieve the rheological properties required for direct ink writing of the support ink. The higher concentration of catalyst in the support ink prevents diffusion of catalyst molecules from the adjacent magnetic inks, and therefore helps prevent imperfect curing of the printed magnetic structures. After the magnetic inks were fully cured upon heating at 120 °C for 1 h, the fugitive support ink was removed by rinsing with isopropyl alcohol using an orbital shaker (Micro Plate Shaker, VWR).

Printing procedure. The prepared magnetic and support inks were loaded into syringe barrels and defoamed at 2,200 r.p.m. for 1 min to remove trapped air bubbles. The inks were then mounted to the custom-designed 3D printer based on a Cartesian gantry system (AGS1000, Aerotech). Conical nozzles with inner diameter 410 μm (Smoothflow Tapered Tip, Nordson EFD) were used for both inks in our demonstrations (Figs. 2 and 3). The detailed designs including ferromagnetic domain patterns and dimensions of the printed structures in Figs. 2 and 3 are given in Extended Data Fig. 6. The external magnetic fields applied at the nozzle to reorient the magnetic particles embedded in the ink during printing were generated by either an electromagnet or a permanent magnet. Printing paths were generated by CAD drawings (SolidWorks, Dassault Systèmes) and converted into G-code by a commercial software package (CADfusion, Aerotech) and custom Python scripts to command the x – y – z motion of the printer head. See Supplementary Video 3 for overall printing and actuation processes.

Rheological characterization. Rheological responses (Extended Data Fig. 2a, b) of the magnetic and support inks were characterized using a rotational rheometer (AR-G2, TA Instruments) with a 20-mm-diameter steel plate geometry. For magnetic inks, both magnetized and nonmagnetized samples were tested to evaluate the effects of magnetic interaction between the embedded magnetized particles. Apparent viscosities were measured via steady-state flow experiments with a sweep of shear rates (0.01–100 s^{-1}). Shear storage moduli were measured as a function of shear stress via oscillation experiments at a fixed frequency of 1 Hz with a sweep of stress (10–10,000 Pa). The magnetic and support inks were equilibrated at 25 °C for 1 min before testing, and all experiments were performed at 25 °C with a gap height of 0.5 mm.

Magnetic characterization. The quality of alignment of the magnetic particles was evaluated by measuring the magnetic moment density (magnetization) of the printed samples with a vibrating sample magnetometer (DMS 1660, ADE Technologies). To prepare specimens, a set of parallel lines was printed in the same direction to construct a rectangular film. Then, the printed film was cut into circles using a 6-mm biopsy punch (MilteX Inc.) to fit into the sample holder of the machine. The magnetic moments of the samples were measured against a sweep of external magnetic fields from $-8,000 \text{ A m}^{-1}$ to $8,000 \text{ A m}^{-1}$. Remanent magnetization, which corresponds to the measured magnetic moment when the applied external field is zero, was divided by each specimen's volume to obtain the magnetic moment density of the specimen.

Mechanical testing. Two types of rectangular planar sheets (width 12 mm, length 35 mm) were printed with an conical nozzle of diameter 840 μm in the absence of external magnetic fields and under applied magnetic fields generated by a permanent magnet around the nozzle, respectively. After curing, the sheets were cut

into dog-bone-shaped specimens with known dimensions (width 4 mm, gauge length 17 mm) for tensile testing. The cross-sectional area of each specimen was calculated by dividing the sample's original volume by its length, where the volume was calculated based on the sample's mass measured before the cut and the density (2.434 g cm^{-3}) of the composite ink containing 20 vol% of NdFeB. The specimens were tested on a mechanical testing machine (Z2.5, Zwick/Roell) with a 20 N load cell at a strain rate of 0.01 s^{-1} . Nominal stress–stretch curves were plotted for both materials, and shear moduli μ were obtained by fitting the experimental curves using a neo-Hookean model (Extended Data Fig. 2c). The shear modulus of the magnetized-ink-based material we obtained was $\mu = 330 \text{ kPa}$. The specimen printed in the presence of external fields showed higher shear modulus compared with the specimen printed without external fields ($\mu = 245 \text{ kPa}$). This higher shear modulus may be attributed to the field-induced alignment of ferromagnetic particles along the filaments when magnetic fields were applied during the printing.

Imaging and videography. Images and videos of the programmed shape changes of the printed samples were taken under a blue LED light source (460-nm wavelength), while applying external magnetic fields in ambient conditions. The external fields were generated by either permanent magnets (K&J Magnetics) or electromagnets (APW Company) depending on the shapes and sizes of the printed samples (Extended Data Fig. 10). Images and videos were taken with a DSLR camera (D7000, Nikon) with a red-coloured filter (HMC R25A, Hoya) that transmits wavelengths above about 600 nm (Supplementary Video 3). To reduce the effects of friction between the printed samples and the substrate, fine glass powders with an average size of 9–13 μm (glass spheres, Sigma Aldrich) were applied to the substrate as a dry lubricant.

Finite-element analysis. For all designs presented in Figs. 1–3, the shapes deformed in the presence of external magnetic fields were simulated using a user-defined element subroutine implemented in the commercial finite-element analysis software ABAQUS. For all simulations, the following input parameters were used: the shear modulus $\mu = 330 \text{ kPa}$, the bulk modulus $K = 1,000\mu$ (the large bulk modulus was chosen to approximate incompressibility), and the uniform external magnetic field $B = 200 \text{ mT}$. For the magnetization parameter in the simulation, the experimentally measured value ($M = 81 \text{ kA m}^{-1}$; see Fig. 1b) was used for samples printed with inks containing 20 vol% of NdFeB particles through nozzles with 410 μm diameter under the applied field of 50 mT at the nozzle tip.

Validation of printing-induced magnetization. The magnetization of a sample printed with a nozzle of diameter 410 μm in the presence of magnetic fields (50 mT) was measured while varying the angular position of the printed fibres with respect to the horizontal direction (Extended Data Fig. 4a). The maximum magnetization value was measured when the printed fibres are aligned with the positive x direction, in which an external magnetic field is applied by the vibrating sample magnetometer. The measured magnetization value decreased as the angle increased and reached almost zero when the printed fibres were vertically aligned. When the specimen was rotated by 180°, the sign of the measured magnetization was changed, indicating that the specimen's magnetic polarity was reversed, while the magnitude remained almost unchanged (Extended Data Fig. 4b). It demonstrates that the printed fibre direction can represent the overall magnetization direction (that is, magnetic polarity) of the printed sample.

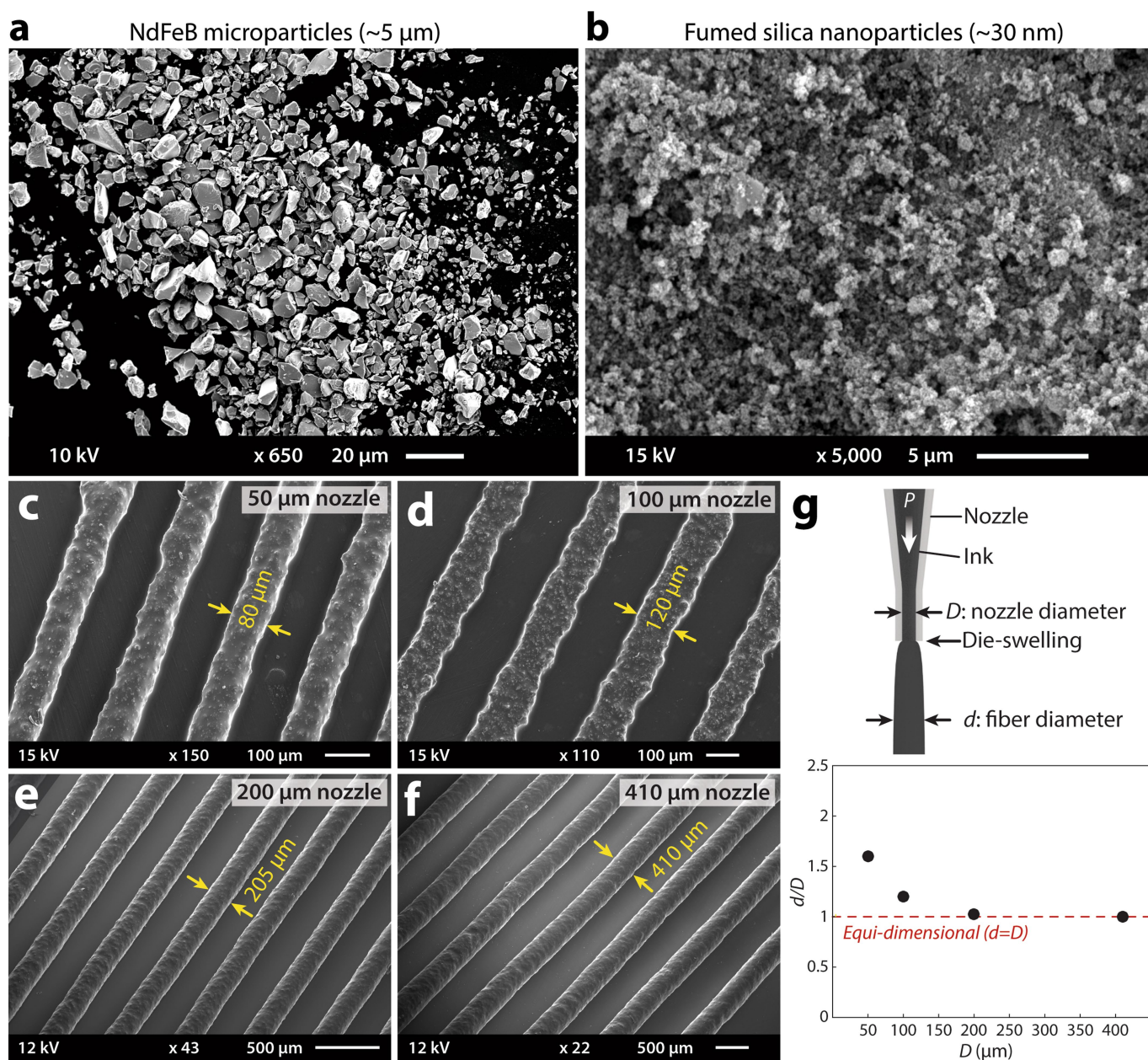
Calculation of energy and power density. As evaluation criteria for actuation performance, we used three quantities that can either be found or calculated from the literature. First, we used the actuation rate $f = 1/t$, where t is the time taken to generate one complete actuation cycle. For materials with irreversible actuation such as shape memory polymers^{27,32}, the actuation rate was considered to be the time taken for completing the first cycle of actuation. Second, we used the energy density ρ_E , which can be determined from force–stroke curves for actuation. Third, we used the power density $\rho_W = f\rho_E$ to evaluate the overall actuation performance of various 3D-printed shape-programmable soft materials. For papers that report force–stroke curves for actuation or the corresponding values of energy density, we used the reported values. When the data were not available, we approximated the values for different classes of materials.

For elastically actuated materials such as shape memory polymers, liquid crystal elastomers and other composite materials, the energy density was approximated as³³ $\rho_E = E(\varepsilon_a)^2/2$ where E is Young's modulus in the rubbery state and ε_a is the actuation strain. For osmotically actuated materials such as hydrogels and other swelling-based actuators, the energy density was approximated as³⁴ $\rho_E = \Delta\Pi\varepsilon_s/2$, where $\Delta\Pi$ is the change in osmotic pressure upon swelling and ε_s is the swelling strain. For magnetically actuated materials with programmed ferromagnetic domains, the energy density was approximated as $\rho_E = 3\mu(\varepsilon_a)^2/2$, where μ is the shear modulus and ε_a is the strain that developed in a deformed state due to the applied magnetic field. The quantities to evaluate the actuation performance were summarized in Extended Data Fig. 8.

Data availability. All data generated or analysed during this study are included in the published article and its Supplementary Information, and are available from the corresponding author on reasonable request.

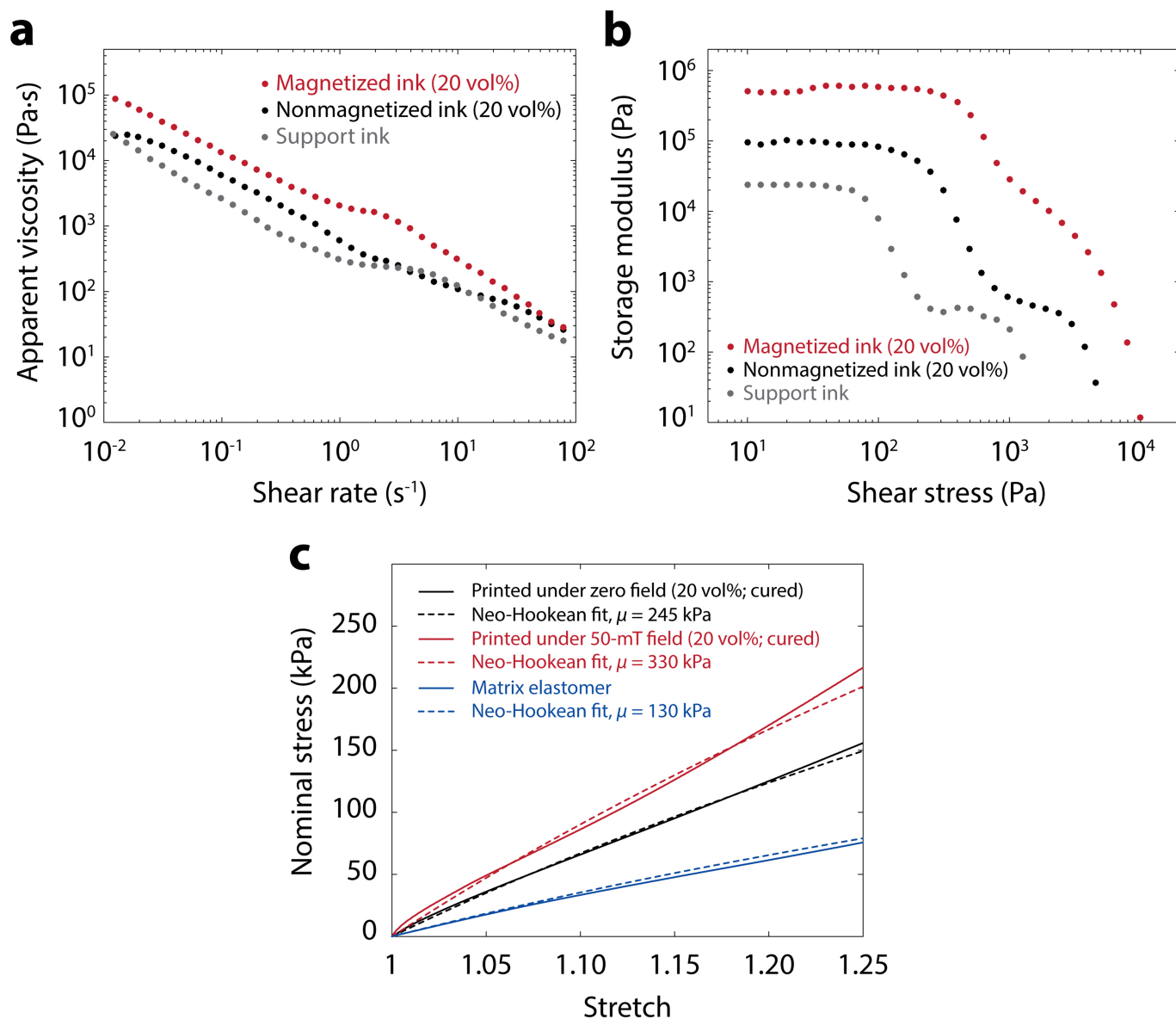
Code availability. The codes for 3D printing and the user element subroutine for numerical simulation are available upon request.

32. Zhang, Q., Zhang, K. & Hu, G. Smart three-dimensional lightweight structure triggered from a thin composite sheet via 3D printing technique. *Sci. Rep.* **6**, 22431 (2016).
33. Mirfakhrai, T., Madden, J. D. & Baughman, R. H. Polymer artificial muscles. *Mater. Today* **10**, 30–38 (2007).
34. Illeperuma, W. R., Sun, J.-Y., Suo, Z. & Vlassak, J. J. Force and stroke of a hydrogel actuator. *Soft Matter* **9**, 8504–8511 (2013).
35. Huang, L. M. et al. Ultrafast digital printing toward 4D shape changing materials. *Adv. Mater.* **29**, 1605390 (2017).
36. Bakarich, S. E., Gorkin, R., Panhuis, M. h. & Spinks, G. M. 4D printing with mechanically robust, thermally actuating hydrogels. *Macromol. Rapid Commun.* **36**, 1211–1217 (2015).
37. Wu, J. et al. Multi-shape active composites by 3D printing of digital shape memory polymers. *Sci. Rep.* **6**, 24224 (2016).
38. Ambulo, C. P. et al. Four-dimensional printing of liquid crystal elastomers. *ACS Appl. Mater. Interfaces* **9**, 37332–37339 (2017).
39. Kotikian, A., Truby, R. L., Boley, J. W., White, T. J. & Lewis, J. A. 3D printing of liquid crystal elastomeric actuators with spatially programmed nematic order. *Adv. Mater.* **30**, 1706164 (2018).
40. Li, W. et al. Flexible circuits and soft actuators by printing assembly of graphene. *ACS Appl. Mater. Interfaces* **8**, 12369–12376 (2016).



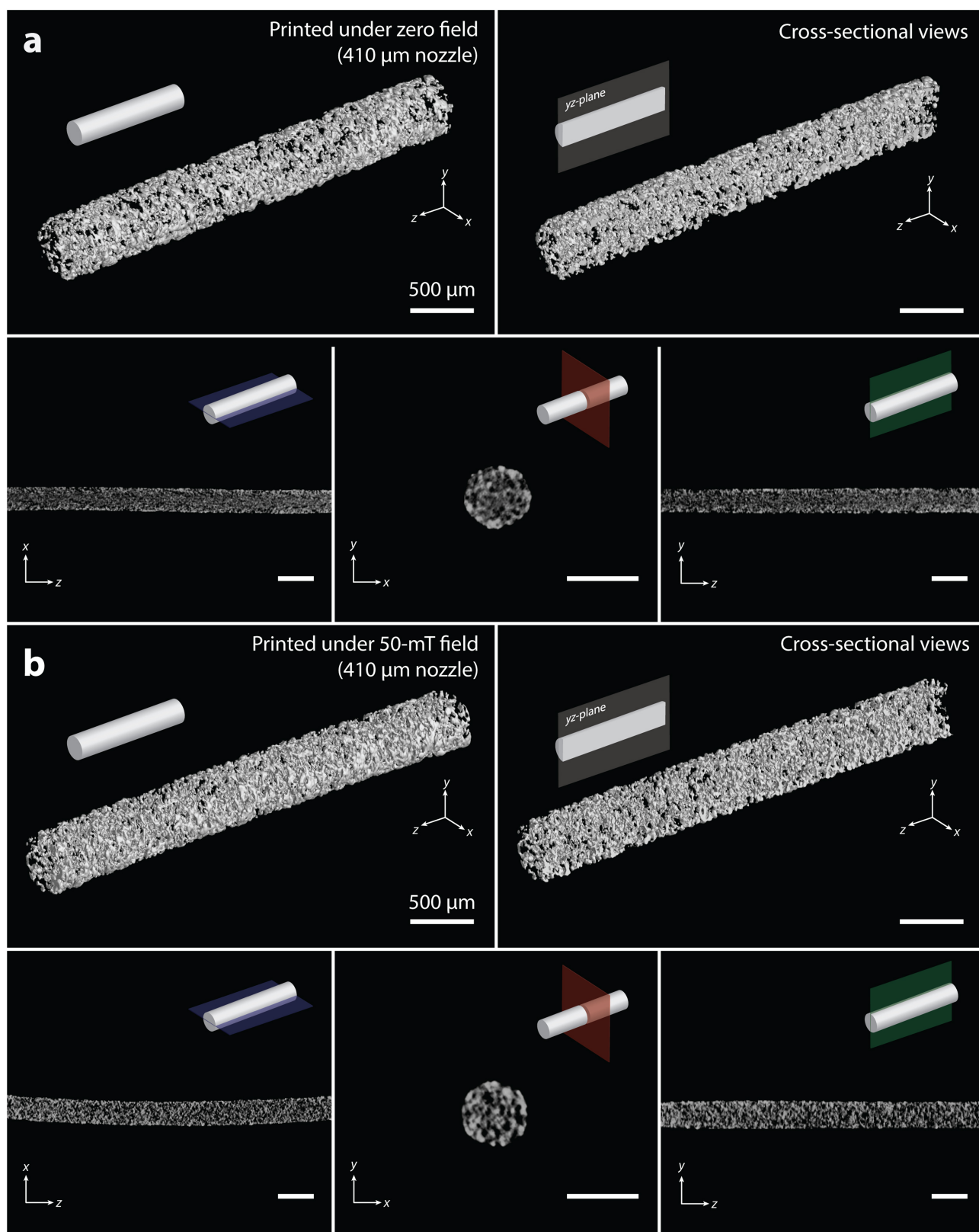
Extended Data Fig. 1 | Scanning electron microscope images of NdFeB and fumed silica particles and printed fibres. **a**, Magnetizable microparticles of NdFeB alloy in flake-like shapes with an average size of $5\ \mu\text{m}$. **b**, Fumed silica nanoparticles with an average size of $30\ \text{nm}$.

c–f, Fibres printed using nozzles with diameters of $50\ \mu\text{m}$ (**c**), $100\ \mu\text{m}$ (**d**), $200\ \mu\text{m}$ (**e**), and $410\ \mu\text{m}$ (**f**). **g**, The ratio between the printed fibre and the nozzle diameter, which is called the die-swelling ratio, plotted against the nozzle diameter.



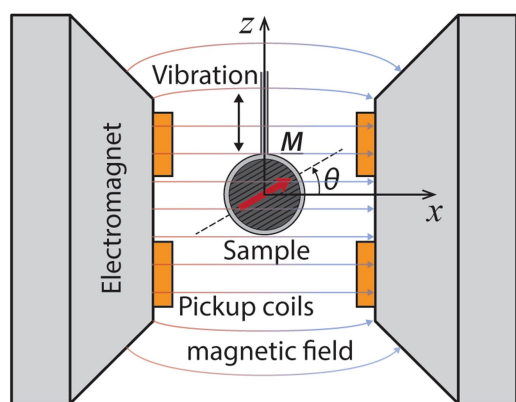
Extended Data Fig. 2 | Mechanical characterizations of the ink and the printed materials. **a**, **b**, Apparent viscosity as a function of applied shear rate (**a**) and storage modulus as a function of applied shear stress (**b**) for 20 vol% magnetized ink (red), 20 vol% nonmagnetized ink (black) and support ink (grey). **c**, Nominal tensile stress–stretch curves (solid lines) for specimens printed with the magnetic ink in the absence of external

fields (black), with applied magnetic fields of 50 mT (red) at the nozzle tip generated by a permanent magnet, and the elastomer matrix with no magnetic particles (blue). The shear modulus μ of each material was obtained by fitting the experimental curves to a neo-Hookean model (dashed lines).



Extended Data Fig. 3 | Micro-computed tomography images of printed fibres. **a**, A fibre printed with a nozzle of diameter 410 μm in the absence of applied magnetic field. **b**, A fibre printed with a nozzle of diameter

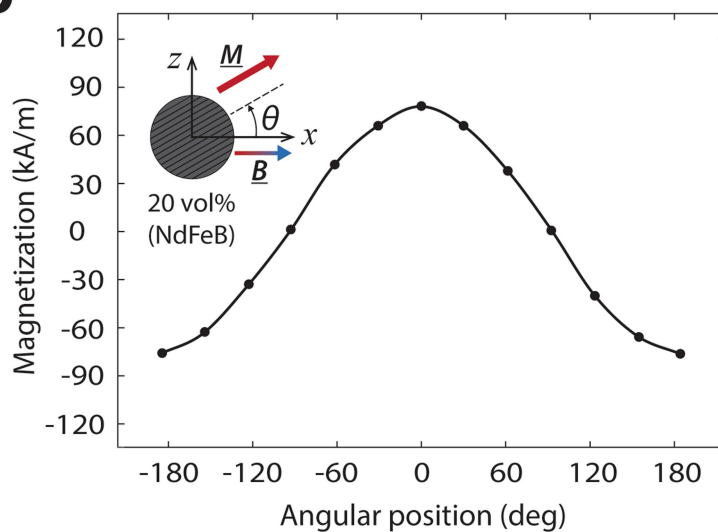
410 μm in the presence of an applied magnetic field of 50 mT at the nozzle tip. No obvious aggregation of ferromagnetic particles in the printed fibres can be observed.

a

Vibrating Sample Magnetometer

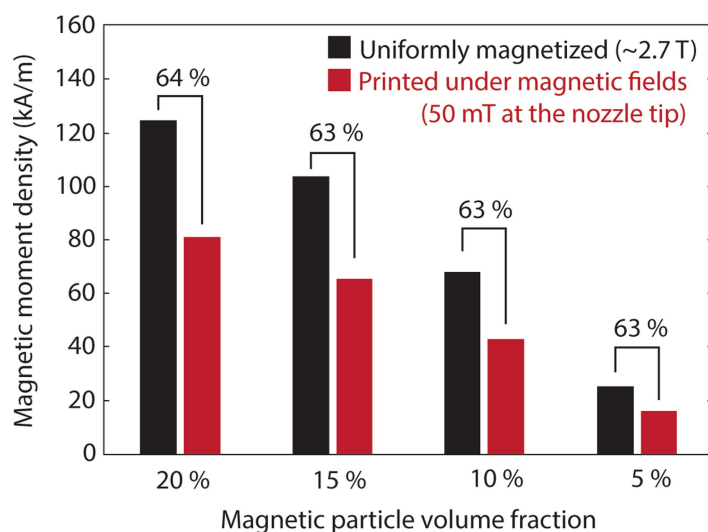
Extended Data Fig. 4 | Experimental validation of the magnetization induced during printing under the applied magnetic field.

a, Experimental setup with a vibrating sample magnetometer for measuring the magnetization of a sample printed with a nozzle of diameter

b

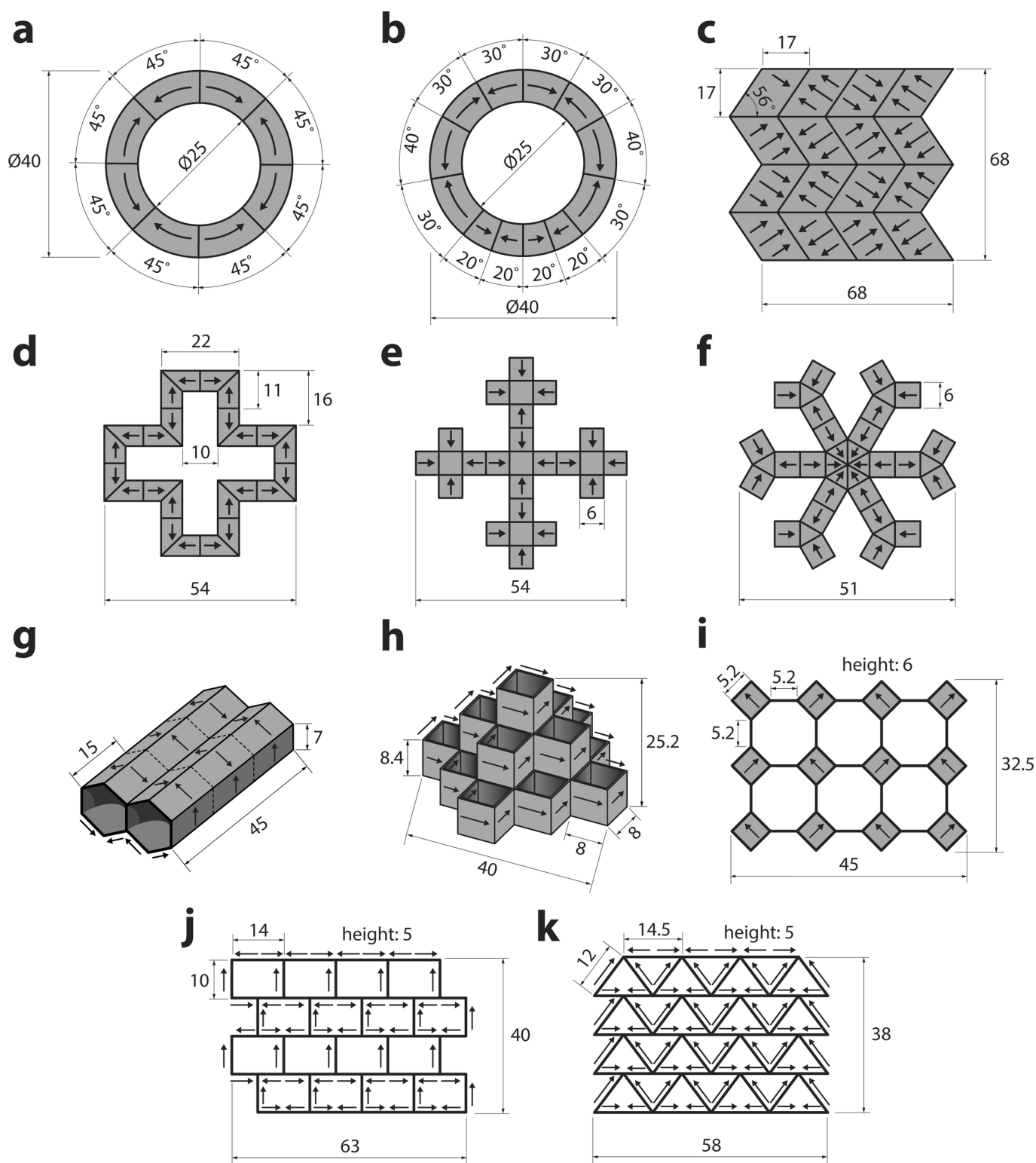
410 μm under the presence of magnetic field of 50 mT at the nozzle tip.

b, Magnetization values measured at various angular positions of the printed fibres with respect to the external magnetic field applied by the vibrating sample magnetometer.



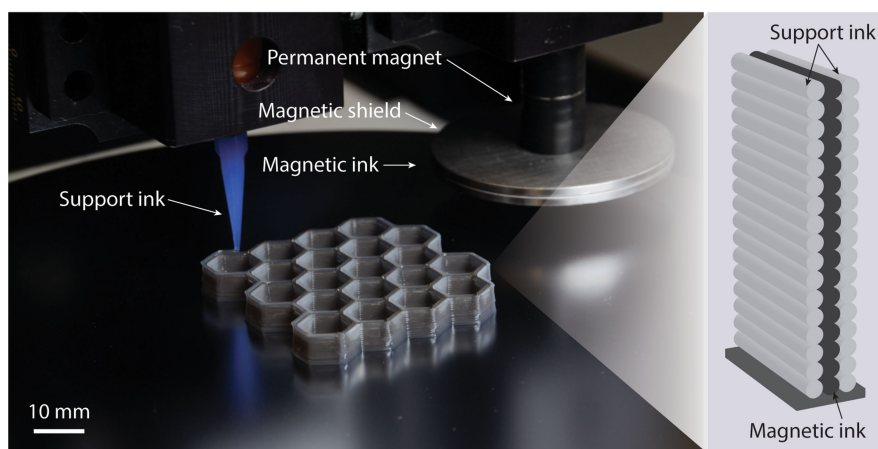
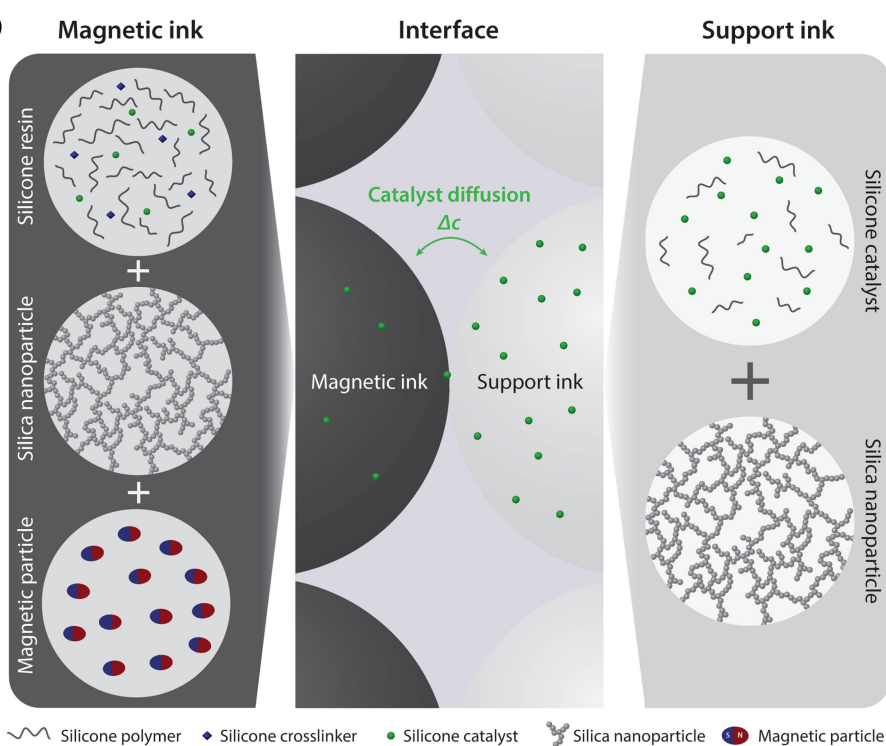
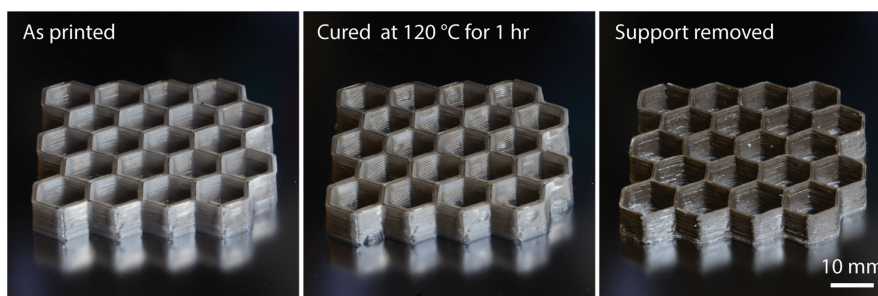
Extended Data Fig. 5 | Magnetic moment densities of printed samples with different NdFeB particle volume fractions. For printed specimens at each volume fraction, a permanent magnet is used to generate external fields (50 mT at the nozzle tip). The magnetization values of printed samples (red) are compared with the maximum achievable magnetization values (black) measured from uniformly magnetized samples. The

uniformly magnetized samples are printed in the absence of external fields, cured, and then magnetized under impulsive fields (about 2.7 T). Printing under the applied field of 50 mT yields a magnetic moment density that corresponds to 63%–64% of the maximum achievable magnetization at each volume fraction of NdFeB particles.



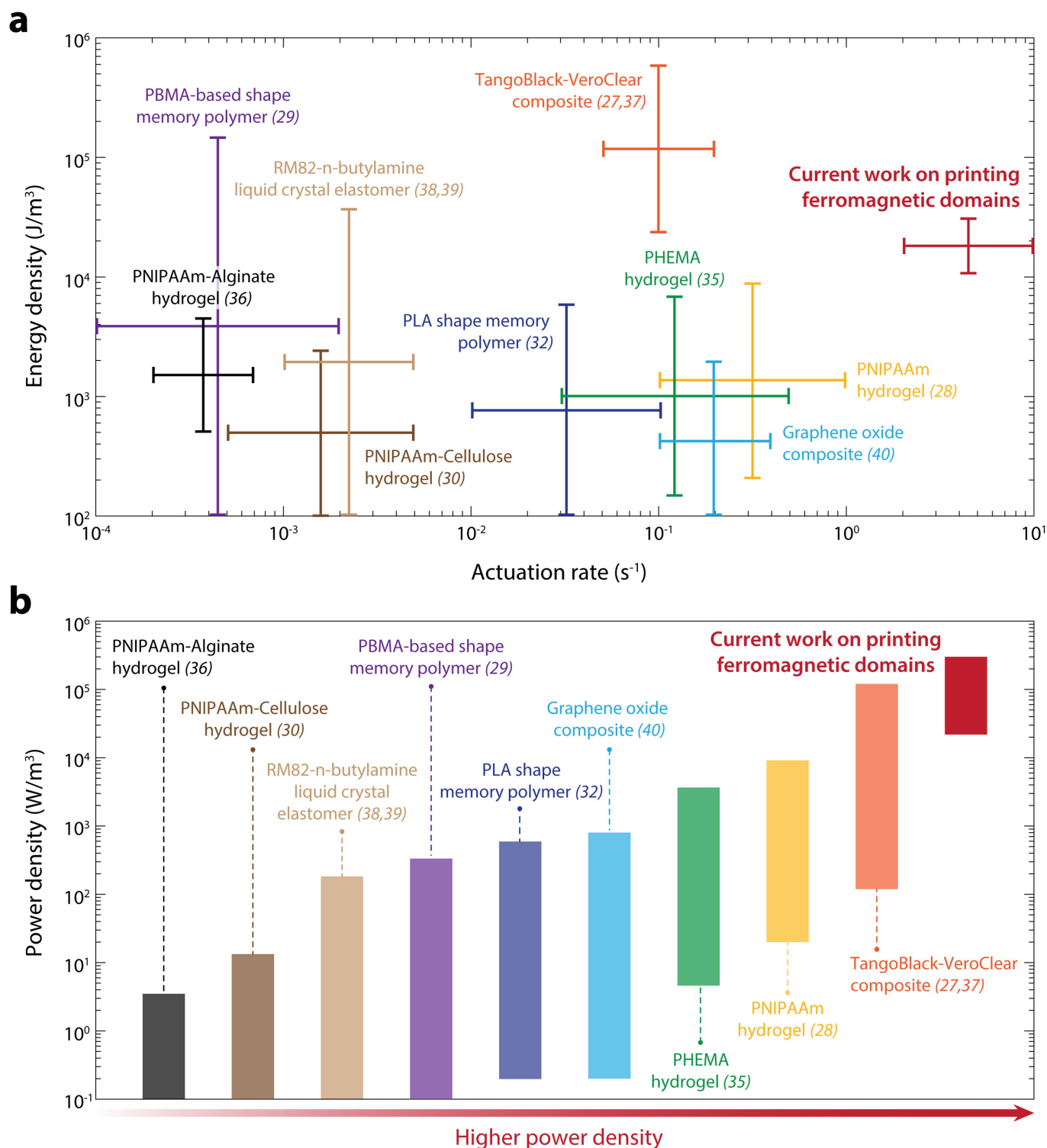
Extended Data Fig. 6 | Schematic designs and dimensions of the two-dimensional and 3D structures in Figs. 2 and 3. **a**, An annulus encoded with alternating domains that are equidistant. **b**, An annulus encoded with alternating domains that vary in size. **c**, A Miura-ori fold encoded with alternating oblique patterns of ferromagnetic domains. **d**, A hollow cross encoded with alternating ferromagnetic domains along the perimeter. **e**, **f**, Quadrupedal (**e**) and hexapedal (**f**) structures enabled by folding of the magnetically active segments surrounding the magnetically inactive

segments. **g**, Two adjoining hexagonal tubes programmed to form undulating surfaces under applied magnetic fields. **h**, A pyramid-shaped thin-walled structure programmed to elongate in its diagonal direction along applied magnetic fields. **i–k**, A set of auxetic structures (with negative Poisson's ratios) programmed to shrink in both length and width under applied magnetic fields. The dimensions in this figure are given in millimetres.

a**b****c**

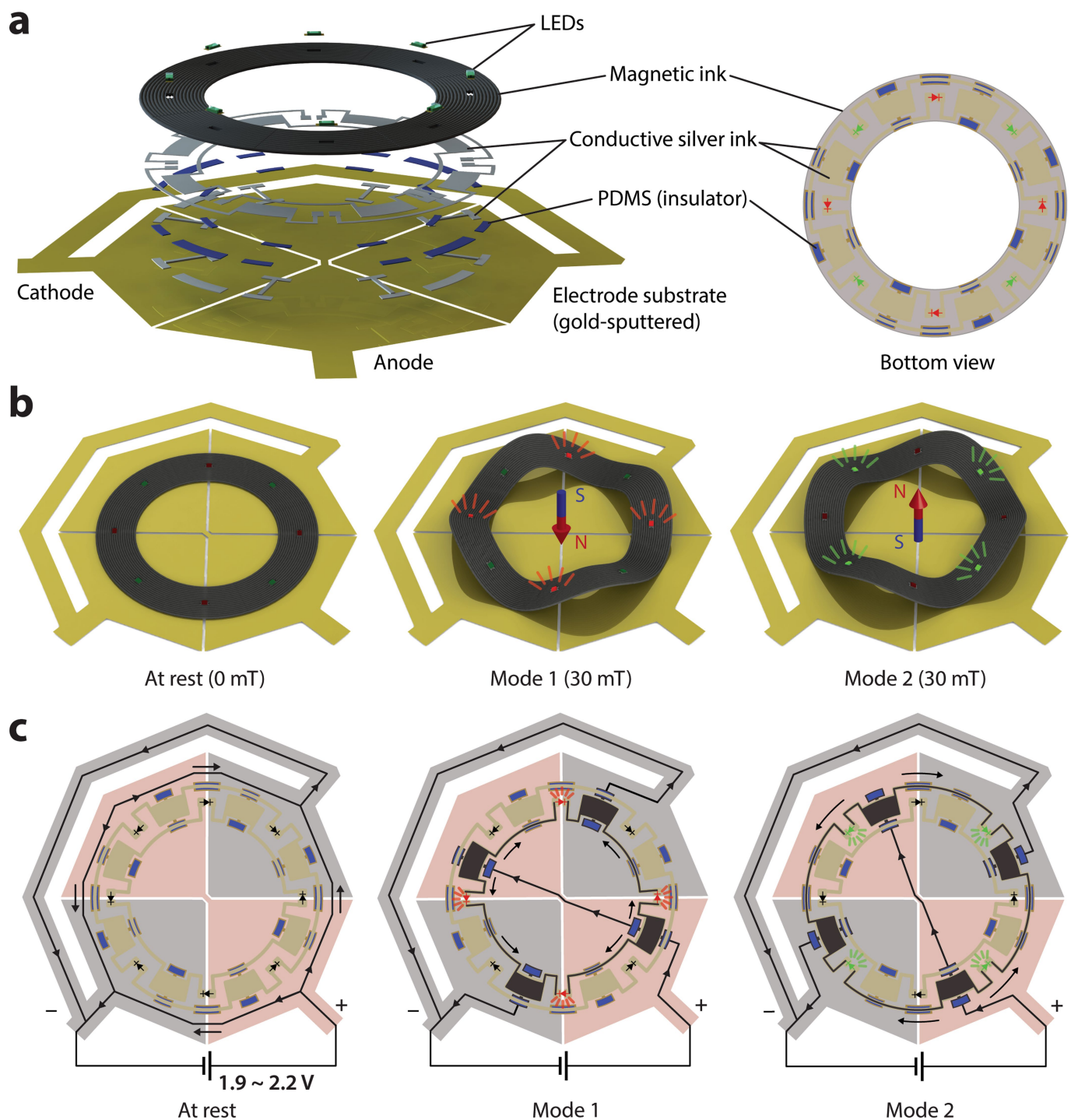
Extended Data Fig. 7 | Overall fabrication process of printing multilayered structures assisted by the use of support inks. a, Printing multilayered hexagonal arrays using magnetic and support inks. The use of support inks as fugitive buttresses enables stacking the deposited magnetic inks stably up to tens or even hundreds of layers. **b,** Chemical composition of magnetic and support inks. The higher concentration of catalyst in the

support ink prevents diffusion of catalyst molecules through the interface and thus prevents imperfect curing of the adjacent magnetic inks. Δc denotes the difference in catalyst concentration between the support and magnetic inks. **c,** The printed magnetic inks are cured by heating at 120 °C for 1 h. The support ink is then removed by solvent rinses.



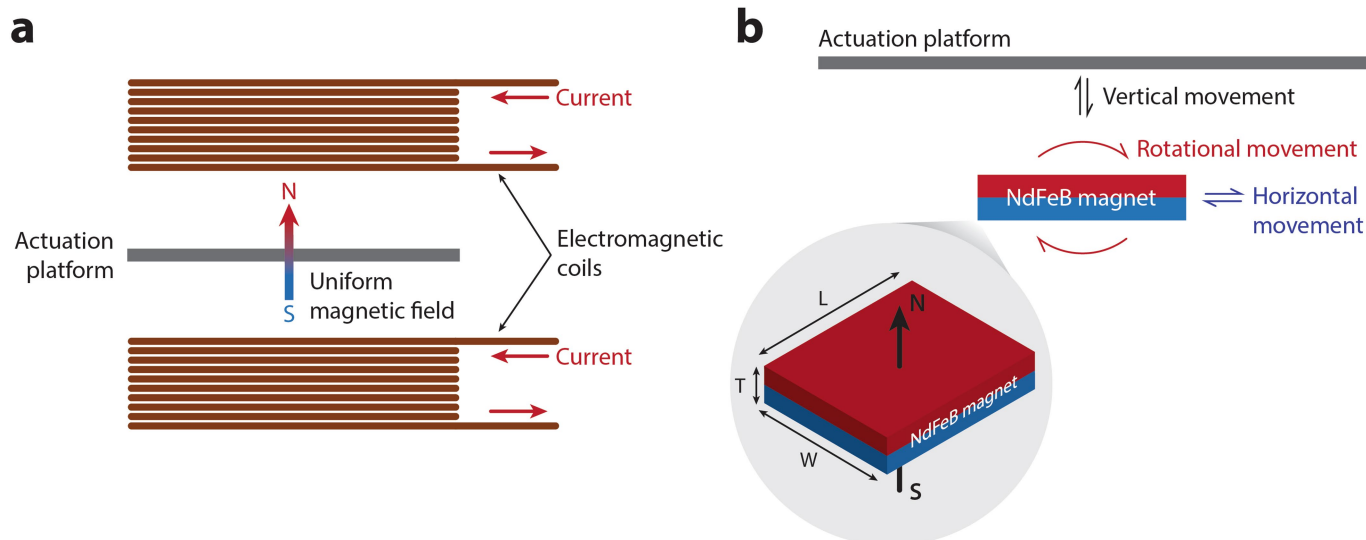
Extended Data Fig. 8 | Actuation performance of 3D-printed shape-programmable soft materials. **a**, Energy density and actuation rate of our magnetically responsive structures presented in Figs. 1–3 are plotted and compared with those of existing 3D-printed shape-programmable soft materials in the literature^{27–30,32,35–40}. **b**, Power density is calculated as energy density multiplied by the actuation rate of each material and plotted for comparison; the materials are listed in order of

increasing power densities. PNIPAAm = poly(*N*-isopropylacrylamide); PMBA = poly(benzyl methacrylate); PHEMA = poly(hydroxyl ethyl methacrylate); PLA = poly(lactic acid); RM82 = 1,4-bis-[4-(6-acryloyloxyhexyloxy)benzoyloxy]-2-methylbenzene. TangoBlack and VeroClear are commercially available acrylic photocurable polymers from Stratasys Ltd.



Extended Data Fig. 9 | Schematic designs and working principles of the reconfigurable soft electronic device demonstrated in Fig. 4a. **a**, Exploded and bottom views of the printed device, in which soft electronic circuitry and components are embedded by means of a hybrid fabrication process based on multimaterial 3D printing. **b**, Two different shapes depending on the direction of applied magnetic fields of 30 mT,

which yield different electronic functions (red micro-LEDs lit up in Mode 1 and green micro-LEDs lit up in Mode 2). **c**, Schematic diagram of the embedded soft electronic circuits, which are designed to turn active only in the designated mode of transformation owing to the selective contact with the gold electrode on the substrate.



Extended Data Fig. 10 | Schematic illustrations of the methods for applying magnetic fields to actuate the printed structures. a, b. The magnetic fields for actuating the printed structures can be applied in two ways. A pair of electromagnetic coils are used to generate a uniform

magnetic field (a). A NdFeB magnet (width 2 in, length 3 in, thickness 0.5 in, surface flux density 300 mT) is used to create spatially varying magnetic fields for dynamic actuation by combining vertical, horizontal and rotational movements of the magnet (b).

In the format provided by the authors and unedited.

Printing ferromagnetic domains for untethered fast-transforming soft materials

Yoonho Kim^{1,2,5}, Hyunwoo Yuk^{1,5}, Ruike Zhao^{1,5}, Shawn A. Chester³ & Xuanhe Zhao^{1,4*}

¹Soft Active Materials Laboratory, Department of Mechanical Engineering, Massachusetts Institute of Technology, Cambridge, MA, USA. ²Harvard-MIT Division of Health Sciences and Technology, Massachusetts Institute of Technology, Cambridge, MA, USA. ³Department of Mechanical and Industrial Engineering, New Jersey Institute of Technology, Newark, NJ, USA. ⁴Department of Civil and Environmental Engineering, Massachusetts Institute of Technology, Cambridge, MA, USA. ⁵These authors contributed equally: Yoonho Kim, Hyunwoo Yuk, Ruike Zhao. *e-mail: zhaox@mit.edu

SUPPLEMENTARY INFORMATION

Printing ferromagnetic domains for untethered fast-transforming soft materials

Yoonho Kim^{1,2,5}, Hyunwoo Yuk^{1,5}, Ruike Zhao^{1,5}, Shawn A. Chester³ & Xuanhe Zhao^{1,4*}

¹Soft Active Materials Laboratory, Department of Mechanical Engineering, Massachusetts Institute of Technology, Cambridge, MA, USA.

²Harvard-MIT Division of Health Sciences and Technology, Massachusetts Institute of Technology, Cambridge, MA, USA.

³Department of Mechanical and Industrial Engineering, New Jersey Institute of Technology, Newark, NJ, USA.

⁴Department of Civil and Environmental Engineering, Massachusetts Institute of Technology, Cambridge, MA, USA.

⁵These authors contributed equally.

*e-mail: zhaox@mit.edu

I. Constitutive law for soft materials with ferromagnetic domains

To quantitatively predict the deformations of printed structures under applied magnetic fields, we develop a constitutive law for soft materials with ferromagnetic domains composed of a silicone elastomer matrix embedded with neodymium-iron-boron (NdFeB) microparticles. Application of magnetic fields induces torques on the embedded ferromagnetic particles, which create stresses that collectively lead to a macroscale material response, causing the whole structure to transform into a configuration that minimizes the combined elastic and magnetic potential energy of the system.

The pure elastic deformation of the soft material is taken to follow the generalized neo-Hookean model (see Extended Data Fig. 2c for validation). The elastic potential energy per unit volume of the soft material in the reference (undeformed) configuration can be expressed as

$$W^{\text{elastic}} = \frac{\mu}{2} (J^{-2/3} I_1 - 3) + \frac{K}{2} (J - 1)^2, \quad (\text{S1})$$

Where μ and K are the material's shear modulus and bulk modulus, respectively, and $I_1 = \text{tr}(\mathbf{FF}^T)$ is the first invariant of the left Cauchy–Green tensor with \mathbf{F} representing the deformation gradient tensor. The quantity J , the volumetric Jacobian of the deformation, is defined as $J = \det \mathbf{F}$. For an incompressible solid, the deformation satisfies $J = 1$.

The magnetic moment density (or magnetization) at a certain point of the soft material in the reference configuration is denoted as \mathbf{M} . Correspondingly, the magnetization vector at the same material point of the soft material, which can be compressible, in the current (deformed) configuration is \mathbf{FM}/J . The magnetic field applied in the space is denoted as \mathbf{B} . Since the permeability of silicone elastomer and NdFeB is close to the permeability of air, we assume that the presence of soft materials with ferromagnetic domains does not substantially alter the applied magnetic field and that the magnetic potential energy from higher order terms of \mathbf{B} and \mathbf{M} are negligible. Based on these assumptions, the magnetic potential energy per unit volume of the soft material in the current configuration can be calculated as $-(\mathbf{FM}/J) \cdot \mathbf{B}$. Correspondingly, the magnetic potential energy per unit volume of the soft material in the reference configuration can be calculated as

$$W^{\text{magnetic}} = -J [(\mathbf{FM}/J) \cdot \mathbf{B}] = -\mathbf{FM} \cdot \mathbf{B}. \quad (\text{S2})$$

Notably, Eq. S2 gives that pure rotation of a ferromagnetic domain in an applied magnetic field can induce magnetic potential energy.

Combining Eqs. S1 and S2, the total potential energy per unit volume of the soft material in the reference configuration is expressed as

$$W = \frac{\mu}{2} (J^{-2/3} I_1 - 3) + \frac{K}{2} (J - 1)^2 - \mathbf{FM} \cdot \mathbf{B}. \quad (\text{S3})$$

Based on work-conjugation, the Cauchy stress tensor $\boldsymbol{\sigma}$ can be obtained from the following relation

$$\boldsymbol{\sigma} = \frac{1}{J} \frac{\partial W}{\partial \mathbf{F}} \mathbf{F}^T. \quad (\text{S4})$$

Substituting Eq. S3 into S4, the Cauchy stress tensor is calculated as

$$\boldsymbol{\sigma} = \mu J^{-5/3} \left(\mathbf{F} \mathbf{F}^T - \frac{I_1}{3} \mathbf{I} \right) + K(J-1) \mathbf{I} - \frac{1}{J} \mathbf{B} \otimes \mathbf{F} \mathbf{M}, \quad (\text{S5})$$

where \mathbf{I} denotes the identity tensor and the operator \otimes denotes the dyadic product, which takes two vectors to yield a second order tensor. Specifically, the elastic Cauchy stress term (the first two terms of Eq. S5) can be expressed as

$$\boldsymbol{\sigma}^{\text{elastic}} = \mu J^{-5/3} \left(\mathbf{F} \mathbf{F}^T - \frac{I_1}{3} \mathbf{I} \right) + K(J-1) \mathbf{I}, \quad (\text{S6})$$

and the magnetic Cauchy stress term (the third term of Eq. S5) can be expressed as

$$\boldsymbol{\sigma}^{\text{magnetic}} = -\frac{1}{J} \mathbf{B} \otimes \mathbf{F} \mathbf{M}. \quad (\text{S7})$$

It is worth noting that $\boldsymbol{\sigma}^{\text{magnetic}}$ can be asymmetric to account for the torques induced by the magnetic field applied on ferromagnetic domains. It is also worth noting that the magnetic Cauchy stress reduces to $\boldsymbol{\sigma}^{\text{magnetic}} = -\mathbf{B} \otimes \mathbf{F} \mathbf{M}$ for incompressible materials.

II. Finite-element model for soft materials with ferromagnetic domains

The constitutive law developed for soft materials with ferromagnetic domains has been implemented as a user-defined element (UEL) subroutine in the commercial finite-element software ABAQUS. In order to validate the finite-element model, we use the model to numerically calculate the deformation of a beam uniformly magnetized along its axial direction and subject to a uniform magnetic field. The applied magnetic field \mathbf{B} is either parallel with (Fig. S1a) or perpendicular to (Fig. S1b) the magnetization \mathbf{M} of the beam. We compare the numerical results with analytical solutions to validate the finite-element model.

1) \mathbf{B} parallel with \mathbf{M}

Consider a rectangular beam with edges aligned with 1, 2 and 3 directions (Fig. S1a). We assume that both \mathbf{M} and \mathbf{B} are aligned with the 1 direction in the reference configuration. The resultant homogeneous uniaxial loading is along the 1 direction, giving principal stretch λ_1 . The other two principal stretches, λ_2 and λ_3 , are along the 2 and 3 directions, respectively. The

symmetry in the 2 and 3 directions gives $\lambda_2 = \lambda_3$. Further assuming the material is incompressible (i.e., $J = \lambda_1 \lambda_2 \lambda_3 = 1$), the deformation gradient tensor has the following form

$$[\mathbf{F}] = \begin{bmatrix} \lambda_1 & & \\ & \lambda_1^{-1/2} & \\ & & \lambda_1^{-1/2} \end{bmatrix}. \quad (\text{S8})$$

Under the assumption of incompressibility, the expression for the total potential energy per unit volume of the soft material in the reference configuration, Eq. S3, becomes

$$W = \frac{\mu}{2}(I_1 - 3) - p(J - 1) - \mathbf{F}\mathbf{M} \cdot \mathbf{B}, \quad (\text{S9})$$

where p is a Lagrange multiplier that reinforces the incompressibility condition. The physical meaning of p is a hydrostatic pressure that can be determined by the boundary conditions. Following Eq. S4, the Cauchy stress for the incompressible material can be expressed as

$$\boldsymbol{\sigma} = \mu \mathbf{F}\mathbf{F}^T - p\mathbf{I} - \mathbf{B} \otimes \mathbf{F}\mathbf{M}. \quad (\text{S10})$$

From Eq. S10, the Cauchy stress along three principle directions can be expressed as

$$\sigma_{11} = \mu \lambda_1^2 - p - \lambda_1 MB, \quad (\text{S11a})$$

$$\sigma_{22} = \sigma_{33} = \mu \lambda_1^{-1} - p. \quad (\text{S11b})$$

The traction-free boundary condition gives $\sigma_{11} = \sigma_{22} = \sigma_{33} = 0$. Subtracting Eq. S11b from Eq. S11a gives

$$(\lambda_1 - \lambda_1^{-2}) = MB / \mu. \quad (\text{S12})$$

The stretch λ_1 as a function of the dimensionless quantity MB / μ is plotted as a solid line in Fig. S1a. When $MB / \mu = 0$, there is no magnetic interaction and thus no deformation in the soft material. When \mathbf{M} and \mathbf{B} are in the same direction ($MB / \mu > 0$), the magnetic stress induces a uniaxial elongation of the body ($\lambda_1 > 1$) along the direction of the applied field. When \mathbf{M} and \mathbf{B} are in the opposite directions, the magnetic stress causes a uniaxial compression of the body ($\lambda_1 < 1$) along the direction of the applied field.

In the finite-element model, we assume that the material is almost incompressible with $K \gg \mu$. For comparison, results from the finite-element model for several values of MB / μ are plotted as circles in Fig. S1a. The simulation results match consistently with the analytical prediction given by Eq. S12, validating the finite-element model for soft materials with ferromagnetic domains.

2) **B** perpendicular to **M**

To further validate the finite-element model, we study another case with **B** applied perpendicularly to **M**, which causes the bending of a beam with small deflection (Fig. S1b). An incompressible solid beam with length L , width W , and height H has a uniform magnetization **M** along its axial or length direction (the 1 direction). A uniform magnetic field **B** is applied along the height direction of the beam (the 2 direction), perpendicular to **M**. One end of the beam is clamped. The magnetic stress induces small deflection of the other end of the beam as the embedded magnetic dipoles attempt to align themselves with the applied magnetic field. Considering small deformation, the only non-zero term of the magnetic Cauchy stress in the incompressible body is calculated as $\sigma_{21}^{\text{magnetic}} = -MB$ from Eq. S7.

The magnetic-field-induced torque $d\tau$ for a small volume dV of the beam is calculated through $d\tau = MBdV \equiv MBWHdx$, with dx being a small length along the axial direction (Fig. S1b). Therefore, the magnetic-field-induced torque at position x on the beam can be calculated as

$$\tau(x) = MBWH(L - x). \quad (\text{S13})$$

This torque distribution along the beam is equivalent to the torque distribution generated by a point force Q applied at the free end of the beam along the direction of applied magnetic field. The magnitude of the equivalent point force Q can be calculated as

$$Q \equiv |d\tau / dx| = MBWH. \quad (\text{S14})$$

The bending stiffness of the beam can be calculated as

$$K_b = 3EI / L^3 \equiv 3\mu WH^3 / (4L^3), \quad (\text{S15})$$

where I is the area moment of inertia, defined as $I = WH^3 / 12$, and E is the Young modulus with the relation $E = 3\mu$ for incompressible materials. Then the deflection at the free end of the beam, or the maximal deflection of the beam δ_{max} , under the point load Q can be calculated through $\delta_{\text{max}} = Q / K_b$ in a dimensionless form as

$$\frac{\delta_{\text{max}}}{L} = \frac{4MBL^2}{3\mu H^2}. \quad (\text{S16})$$

For small deflections (e.g., $\delta_{\text{max}} / L < 10\%$), Eq. S16 gives a linear relation between the dimensionless quantities MB / μ and δ_{max} / L . Assuming $L / H = 10$, Eq. S16 is plotted as a black solid line in Fig. S1b. For comparison, the deflections of the beam for a number of prescribed values of MB / μ have been calculated with the finite-element model using an almost incompressible materials (i.e., $K \gg \mu$) and plotted as red squares in Fig. S1b. The analytical and finite-element results show good agreement, validating the finite-element model for soft materials with ferromagnetic domains.

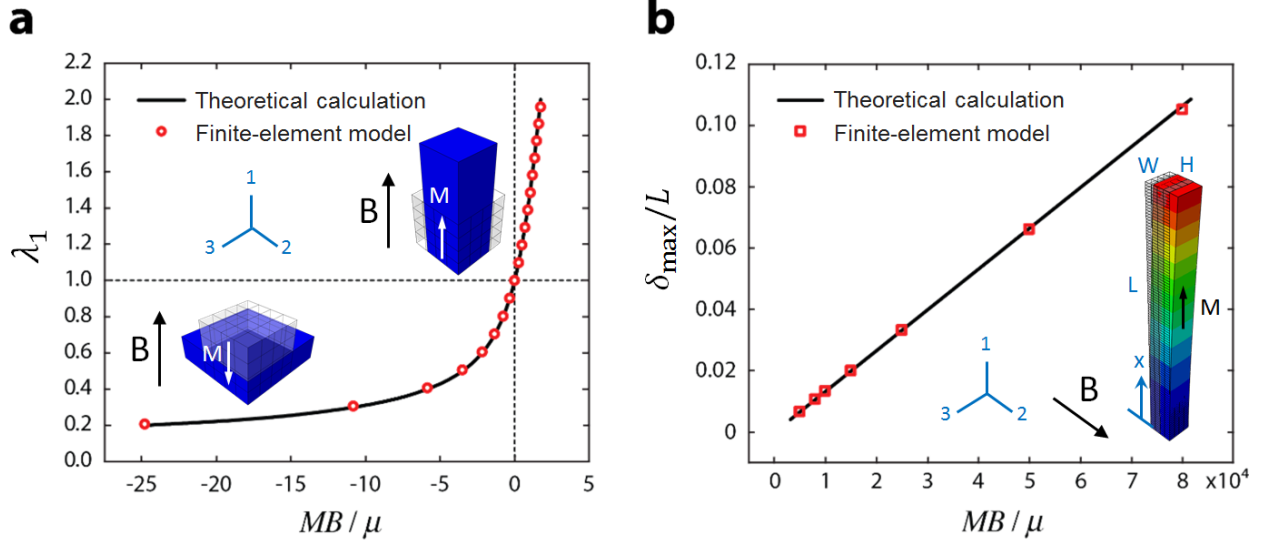


Figure S1 | Validation of the finite-element model based on the constitutive law for soft materials with ferromagnetic domains. a, Comparison of the simulation results from finite-element model (red circles) and theoretical prediction (black solid line) of magnetic-stress-induced stretch λ_1 as a function of the dimensionless quantity MB/μ , when the magnetic field \mathbf{B} is applied in parallel with the magnetization \mathbf{M} possessed by the incompressible neo-Hookean solid with the shear modulus μ . **b**, Comparison of the simulation results from finite-element model (red squares) and theoretical prediction (black solid line) of the deflection at the free end of a slender beam with magnetization \mathbf{M} along its axial direction, when the magnetic field \mathbf{B} is applied along the height direction of the beam (perpendicularly to \mathbf{M}).

III. Scaling analysis of magnetic actuation of beam structures

To quantitatively understand the effects of physical parameters on the magnetic actuation of printed beam samples, we further analyze the bending of the beam illustrated in Fig. S1b. Assuming a small deflection of the beam, the curvature of the deformed beam can be calculated as

$$\kappa(x) = \frac{\tau(x)}{EI}. \quad (\text{S17})$$

Given that $I = WH^3/12$ and $E = 3\mu$ for incompressible materials and Eq. S13, the curvature can be further expressed as

$$\kappa(x) = \frac{4MB(L-x)}{\mu H^2}. \quad (\text{S18})$$

From Eq. S18, we can find that the maximum curvature, which occurs at the base of the beam ($x = 0$), scales as

$$\kappa_{\max} \propto \frac{MBL}{\mu H^2}. \quad (\text{S19})$$

From Eq. S16 in Section II of the supplementary information, we can find that the maximum deflection of the beam, which occurs at the free end of the beam ($x = L$), scales as

$$\delta_{\max} \propto \frac{MBL^3}{\mu H^2} \quad (\text{S20})$$

We can infer from Eq. S20 that there are a number of strategies to achieve effective actuation that yields a large curvature and/or deflection of an axially magnetized beam. A more straightforward approach is to increase either the magnetization strength M or the actuation field B . The magnetization strength M can be increased by either increasing the volume fraction of ferromagnetic microparticles or by increasing the applied field strength during the printing process. Another strategy is to increase the length-to-height ratio L/H by printing more slender fibers when constructing a shape-morphing structure. The last strategy is to reduce the material's shear modulus μ , which can be achieved by reducing the crosslinking density of the elastomer matrix of the composite ink.